Lattice Boltzmann study of mass transfer for Bretherton/Taylor bubble train flow

April 29, 2012

Abstract

This work presents a thorough procedure of how to determine the volumetric mass transfer coefficient in the context of lattice Boltzmann simulations for the Bretherton/Taylor bubble train flow. In this work we address the situation when the hydrodynamic pattern changes from having a vortex in slug ($Ca < 0.7$) to not having it ($Ca > 0.7$) [1]. For the latter case the bubble shape is not symmetric and cannot be approximated through flat surfaces and circumferences as it is done in literature [3, 4]. For $Ca < 0.7$ where there is a vortex in the slug the tracer is well mixed. Thus, it is common to use periodic boundary conditions and the inlet/outlet averaged concentration as the characteristic concentration, Eq. 4. The later is not valid for flows where tracer is not well mixed, i.e. $Ca > 0.7$. This work through examination of different boundary conditions and different characteristic concentration definitions establishes the procedure to determine the volumetric mass transfer coefficient for flows with the capillary number $0.1 < Ca < 1.0$. With simulations of a few unit cells the connection between time (used in simulations) and space (used in experiments) domains is established. The following boundary conditions were examined: periodic boundary conditions, open boundaries, and a few unit cells open boundary simulations. It was shown that the time dependent average concentration to be a characteristic concentration produce robust results, though a bit overpredicted. The inlet/outlet flux averaged concentration [3] to be a characteristic concentration produce unreliable results in the range of capillary numbers specified. In comparison with works [3, 4] where only one unit cell was simulated, a few unit cells open boundaries conditions resemble physical situation most closely. However, they are harder to be conducted but provide the volumetric mass transfer coefficient based only on the spatial information for the capillary number $Ca > 0.7$. We show that all presented in literature strategies are extreme limits of one equation, Eq. 17. Finally, simulation results for different Peclet numbers are compared with analytical predictions presented by van Baten and Krishna [3] and shows a good agreement. The work is of use to people performing mass transfer numerical simulations for bubble train flow in microchannels and/or within the lattice Boltzmann model context.

1 Introduction

The monolith reactors during last years are getting more attention as a promising alternative to slurry reactors and trickle bed reactors [4, 5]. Reactors usually operate in the Bretherton-Taylor regime [6, 7] which describes a flow through a liquid medium of equally sized, long air bubbles, see Fig. 1. This flow regime is characterized by surface tension dominance over inertia and viscous effects, and by comparatively small gas flow velocities [8]. Due to surface tension dominance bubble train flow exhibits advantageous properties which can not be achieved in its macroscopic counterparts: liquid thin films [6] between bubbles and walls remarkably enhance mass transfer from gas and walls to liquid; the plug flow regime occurring in monolith reactors allows to perform chemical reactions in slugs only [4]. Moreover, the low slip velocity between gas and liquid is utilized in the experiments to measure liquid velocity [7]: bubbles travelling with approximately the same velocity as liquid can be captured with a camera. Overall, nowadays one can find a large number of applications of the Bretherton-Taylor bubble train flow: continuous flow analyzers to measure liquid velocity, lung openings, chemical reactions as hydrogenation of nitroaromatics, 2-ethylhexenal, Fischer-Tropsch synthesis, etc. Extensive reviews of Kreutzer et al. [4], Yue et al. [8], Gupta et al. [9] cover a significant number of applications.

This work is focused on the gas to liquid mass transfer study for the Bretherton/Taylor flow. The good understanding of mass transfer and how it depends on the parameters as the capillary number, the Reynolds number, slug and bubble lengths allows to properly manufacture a microchannel with necessary properties to ensure that chemical reactions are performed in the best manner. The mass transfer coefficient characterizing mass transfer is defined as the flux from the surface divided on the concentration difference between the concentration imposed on the body and the characteristic concentration in the domain. The characteristic concentration in the domain significantly depends on underlying hydrodynamics fields. For example, experimental studies [5, 8] show a complex dependency of the mass transfer coefficient on flow parameters: bubble and slug lengths, bubble velocity, which are in turn depend on the capillary number Ca and the Reynolds number Re. Yue et al. [8] established an experimental correlation for the volumetric mass transfer coefficient for a bubble train as a function of the diffusion coefficient, slug and bubble lengths, and bubble velocity:

$$k_L\, a = \frac{2}{d_h}\Big(\frac{D U_{\text{bubble}}}{L_{\text{bubble}} + L_{\text{slug}}}\Big)^{0.5}\Big(\frac{L_{\text{bubble}}}{L_{\text{bubble}} + L_{\text{slug}}}\Big)^{0.3}, \qquad (1)$$

where $k_L\, a$ is the volumetric mass transfer coefficient, d_h is the hydrodynamic capillary diameter, L_{bubble} is the bubble length, L_{slug} is the slug distance (between bubbles), U_{bubble} is the bubble velocity, D is the diffusion coefficient.

Thus, the understanding of mass transfer for the bubble train flow is not possible without deep understanding of hydrodynamic patterns. There are a number of studies available for the hydrodynamic study of the bubble train flow: experimental [10–12] and numerical [1, 13–15]. For the flow of long bubbles between parallel plates chosen here as the study case, it is indicated that there

exists a vortex in the liquid slug for $Ca < 0.7$, see Fig. 8. As well, the bubble shape for low capillary numbers ($Ca < 0.1$ [12]) is symmetric. Thus, in the case of flow between plates for $Ca < 0.1 \div 0.7$ the bubble shape can be represented as two hemicircles and two planar interfaces with the vortex existing in the liquid slug. This is heavily utilized for mass transfer analytical estimations.

As mentioned, the mass transfer coefficient is defined as the mass flux from a certain area, Eq. 4. Thus, analytical estimations [4, 16] are based on decomposition of the bubble shape. The mass transfer coefficient is calculated through two separate contributions from two films and two hemicircles. For both contributions the Higbie penetration theory [17] is utilized, which states that the mass transfer coefficient for simple geometry flow depends on the average time of liquid packet interaction with a geometrical feature. It can be calculated as $\sqrt{\frac{\pi D}{t_{\text{char}}}}$, where t_{char} is the interaction characteristic time, ~~D is the diffusion coefficient~~. As the example for the Higbie penetration theory, the mass transfer coefficient for the flow of bubbles between parallel plates is calculated as (similarly to work of van Baten and Krishna [3]):

$$k_L = 2\sqrt{\frac{\pi D}{t_{\text{film}}}} + 2\sqrt{\frac{\pi D}{t_{\text{circle}}}}, \tag{2}$$

where $t_{\text{film}} = \frac{L_{\text{film}}}{U_{\text{bubble}}}$ states for the interaction time of liquid traveling through planar part of the bubble, $t_{\text{circle}} = \frac{\pi R_{\text{circle}}}{U_{\text{bubble}}}$ is the time which liquid in the slug travels the distance of half bubble circumference.

Despite the simplicity, analytical expressions work well for flows with low capillary numbers $Ca < 0.1$ [5] where the bubble shape is symmetrical and can be nicely approximated. Moreover, because of the hydrodynamic pattern in the slug, i.e. there is a vortex in slug, one can estimate the time for fluid batch to travel whole circumference. However, with the change of the capillary number the situation drastically changes. The symmetrical bubble shape changes ~~and resembles~~ a bullet [18]. With the change of the shape and for flows with $Ca > 0.7$ there is no vortex in the liquid slug. In this case the Higbie theory fails to estimate ~~contribution from bubble caps~~. Thus, the need of numerical simulations where all hydrodynamics fields and complicated bubble shapes are taken in the account is obvious.

However, available numerical studies of mass transfer [3, 4] are ~~lacking~~ the simulation of bubble shapes. The usual simulation of the mass transfer is performed as follows:

I The bubble shape is calculated either through analytical correlations [6] or experimental correlations [12] without directly resolving bubbles shapes through multiphase simulations. The expressions for bubble shapes are available only for flows with the capillary number $Ca < 0.1$.

II Hydrodynamics fields are then obtained by performing simulations of one-component flow around the droplet by imposing the bubble velocity on the walls. Thus, the simulations are performed in the reference frame moving with the bubble. The stress free condition is imposed at the bubble surface.

III The mass transfer simulations are performed in the reference frame moving with the bubble. The saturation concentration is imposed at the bubble surface. Only one unit cell with one bubble in it is used for simulations. Periodic boundary conditions are utilized to determine the volumetric mass transfer coefficient, which is calculated through the following equation [3]:

$$k_L\, a = \frac{\overline{\text{Flux}}}{C_{\text{bubble}} - \langle C_{\text{outlet}} \rangle} \frac{\text{bubble surface area}}{\text{unit cell volume}}, \tag{3}$$

where $\langle C_{\text{outlet}}(t) \rangle = \int C U_{\text{outlet}} \mathrm{d}A / \int U_{\text{outlet}} \mathrm{d}A$ is the averaged in space outlet concentration as the function of time, used as the characteristic concentration in the definition, Eq. 4. The averaged in time concentration flux ($\overline{\text{Flux}}$) is calculated as the difference between the overall average concentration in the whole domain ($\langle C_{\text{overall}} \rangle = \int_V C \mathrm{d}V/V$) at time t_1 and at time t_2 divided on the time difference $t_2 - t_1$. The agreement between numerical simulations [3] and correlations of Bercic and Pintar [5] was good.

There is a certain critics towards the presented numerical approaches [3, 4]. They mainly originate from the bubble shape approximation. It is taken symmetrical, i.e. consisting from hemispheres and cylinder film for the case of flow in circular capillaries. This is valid for small capillary numbers ($Ca < 0.1$.) As it was discussed, for such capillary numbers in the reference frame moving with the bubble there is a vortex in slug. Thus, the tracer is well mixed in slug. The choice of the characteristic concentration needed for the mass transfer coefficient, Eq. 4, in this case is obvious. With small differences in results it can be either averaged in the liquid slug concentration or the outlet space averaged concentration, as used in formulation of van Baten and Krishna [3]. Another critics is towards periodic boundary conditions to calculate the mass transfer coefficient. While it is clear to use periodic boundary conditions for the calculation of hydrodynamics fields for long bubbles motion in the microchannel, it is not the case for mass transfer simulations. Experimental correlations [5] show that the concentration along the streamwise direction changes as the exponential function. However, mass transfer simulations are made only for one unit cell using the periodic boundary conditions with the same concentration at the inlet and at the outlet. The question how one unit cell simulation corresponds to experimental measurements arises where concentration difference is measured at the distances of at least of a few unit cells difference [5]. In other words one needs to understand how the discrete one unit cell simulation corresponds to the continuous picture in experiments where one does not distinguish bubbles but takes measurements of concentration at different locations.

Addressing situations for a rich number of hydrodynamic patterns, shapes, effects for a bubble train we feel that there is a need to examine more carefully the strategies and assumptions which stay behind the mass transfer coefficient numerical simulations. We aim at establishing numerical simulations procedures as to how properly obtain the mass transfer coefficient via a study of different

boundary conditions, different characteristic concentration definitions. The case we want to examine is the two-dimensional case of the bubble train flow between parallel plates. The following issues will be addressed:

I Applicability of periodic boundary conditions to determine the mass transfer coefficient when there is a change of pattern from having vortex in the slug to not having it.

II Validity to use the inlet/outlet averaged or domain averaged concentrations as characteristic concentrations in the definition of the mass transfer coefficient.

III Transition of the continuous experimental picture to numerical simulations of a few unit cells mass transfer. This is the question about connection between time and space domains. In experiments the characteristic concentration is taken as an average in time, but in numerical simulations [3] the characteristic concentration is taken as an average in space.

IV How the change of the hydrodynamic pattern ($Ca > 0.7$) influences mass transfer.

Note that the goal of this paper is to establish procedures and boundary conditions used for the mass transfer coefficient determination. Though at the end of the manuscript we present a comparison of the volumetric mass transfer coefficient on the Peclet number with analytical [16] and experimental correlations [8], the thorough determination of the Sherwood number as a function of other non-dimensional parameters as gas holdup, bubble/slug lenghts, the capillary number is the goal of the future work.

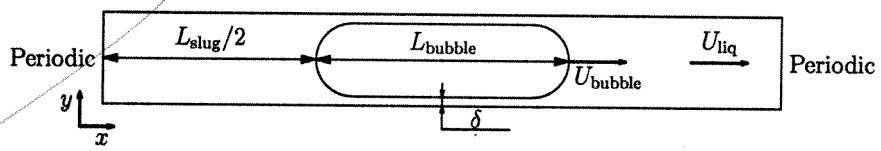

Figure 1: Simplified sketch of the bubble train motion. Using periodic conditions for the velocity field is natural, but needs validation for the mass transfer.

To establish numerical procedures we performed multiphase simulations [14, 18] for the range of capillary numbers $Ca = 0.1 \div 1.0$ to extract bubble shapes. For this range of capillary numbers we are able to capture the bubble shape change and the change of hydrodynamic patterns. The mass transfer simulations were performed with different boundary conditions (open, periodic) and with a few unit cells (1 to 10 unit cells). The numerical approach we take is the lattice Boltzmann method, a relatively new CFD competitor emerged during last 20 years [19–22]. During years the method was applied to simulate not only hydrodynamic problems [23], but as well multiphase flows [24–26], heat transfer [27, 28], ferrofluids [29, 30].

The mass transfer problems in the lattice Boltzmann framework were mainly addressed in series of works of Ginzburg and co-authors [31–33]. However, all these works are of general nature to simulate the advection-diffusion equation via the lattice Boltzmann framework. In comparison, this work focuses on the application side as to establish the procedure of how to obtain the volumetric mass transfer coefficients for bubble train flow. One should mention the work of Yoshino and Inamuro [34] about heat and mass transfers in porous media and the work of Derksen [2] simulates lateral mixing in cross-channel flow. While two last works are focused at particular mass transfer problems, both problems are of homogeneous nature and do not guide as how to obtain the mass transfer coefficient for non-homogenous problems.

The paper is organized as follows. We start with definitions of the volumetric mass transfer coefficient and apply them for the bubble train flow to derive expressions to connect space and time domains. Then the lattice Boltzmann model used to simulate mass transfer is presented followed by benchmarks. Finally, numerical simulations of different boundary conditions and a few unit cells simulations for different hydrodynamic patterns are presented to establish the thorough procedure to determine the volumetric mass transfer coefficient. The comparison with analytical correlations is also presented.

2 Mass transfer definitions

By the definition the mass transfer coefficient from the surface with the imposed constant concentration C_{bubble} is the following:

$$k_L = \frac{\dot{m}}{P\Delta C}, \tag{4}$$

where $\dot{m}$ is the mass rate $\left[\frac{kg}{s}\right]$, P is the area of the surface $\left[m^2\right]$, ΔC is the concentration difference between the surface and the surrounding medium $\left[\frac{kg}{m^3}\right]$. Therefore, k_L has a dimension of velocity $\left[\frac{m}{s}\right]$. Usually, the surrounding medium concentration is taken at the infinite distance from the bubble. However, in the case of complicated geometries and non-homogeneous concentrations, the medium concentration can be the average concentration in the domain or the flux averaged concentration at the inlet or outlet, etc. Thus, one needs to establish a thorough definition of the volumetric mass transfer coefficient in the case of complex geometries and non-trivial hydrodynamic velocity patterns.

There are different methods to estimate the mass transfer coefficient k_L. We first examine the theoretical definitions of the mass transfer in case of point mass sources.

2.1 Point mass sources

In what follows we will present three approaches to calculate point mass transfer coefficients (by point source we assume the source with the infinitesimally small

surface area P):

1. Let us look at the infinitesimal small domain of the volume $A\Delta x$ not moving and with the point mass source. Then the concentration difference can be found as $\Delta C = C^* - C(t)$, where C^* is the imposed point source concentration, $C(t)$ is the time dependent concentration, which do not depend on the location due to homogeneity. Therefore, one can write the time dependent ODE for the concentration in the domain:

$$\dot{m} = A\Delta x \frac{\mathrm{d}C}{\mathrm{d}t} = k_L P(C^* - C(t)), \tag{5}$$

with the initial condition $C(0) = 0$ The solution can be found by solving the ODE:

$$C(t) = C^*(1 - \exp(-k_L\, at)), \tag{6}$$

where $k_L\, a$ is the volumetric mass transfer coefficient defined as:

$$k_L\, a = k_L \frac{P}{A\Delta x} = k_L \frac{P}{V}, \tag{7}$$

where P is the source surface, V is the unit cell volume.

2. Let us predict mass transfer happening in moving with the velocity U liquid, see Fig. 2.

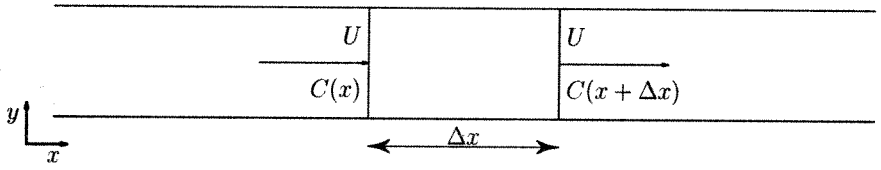

Figure 2: The mass transfer in the moving liquid.

If one can assume that the mass point sources are distributed in the whole medium, then the mass accumulated in the unit volume $V = A\Delta x$ can be calculated as the difference of mass fluxes entering and leaving domain $U\big(C(x + \Delta x) - C(x)\big)$. The accumulated mass should be proportional to the mass transfer coefficient:

$$U\big(C(x + \Delta x) - C(x)\big) = k_L P\big(C^* - C(x)\big), \tag{8}$$

giving the same equation but only in the coordinate domain:

$$C(x) = C^*\Big(1 - \exp\big(-k_L a \frac{x}{U}\big)\Big). \tag{9}$$

Note that the concentration $C(x)$ does not depend on time.

3. If one transfers to the frame moving with the liquid velocity U, then the situation will be the same as in the first case. However one can connect the time and spatial location with the velocity U ($t = \frac{x}{U}$) to obtain the same equation as in the case 2.

2.2 Bubble train

In the application to the bubble train flow, it is useful to think of one bubble to be a point source to make all considerations above valid. For example, the expression (9) was used in the experiments by Bercic and Pintar [5]. However, one should be accurate with the definition of velocities because two different phases co-exist in the bubble train flow. Usually, one can take the velocity U to be as a bulk velocity or $U = U_{\text{gas}} + U_{\text{liq}}$, where U_{gas} and U_{liq} are liquid and gas superficial velocities correspondingly.

Thus, the experimental measurements are straightforward as measuring concentrations at different locations and calculating the volumetric mass transfer coefficient through the logarithmic function. However, if one wants to analytically or numerically calculate the mass transfer coefficients, the situation is much more complicated because of two phases presence and complicated bubble geometry. As it was mentioned before, depending on the capillary number the mixing velocity pattern is different. Analytical approaches [3, 16] assume that the contributions from film and bubble caps can be calculated separately. However, one can see that such an assumption (slug well mixed and the concentration is uniformly distributed over the slug) usually overpredicts the mass transfer [16]. This happens since some tracer concentration from film is mixed with the slug and increases the overall concentration in the slug. Thus, it decreases the mass transfer from bubble caps. Therefore, all estimations for the analytical mass transfer coefficient calculation do not account for mutual mass transfer from neighbouring bubbles.

Another issue is that if the bubble is long enough then the film saturates with the tracer concentration and its influence on mass transfer can be negligible [3]. Mixing patterns of the film and liquid slugs are of great importance for the analytical estimation of mass transfer [8]. However, the assumptions usually taken for the mass transfer calculation are small capillary numbers and certain mixing patterns which help to estimate the mass transfer using the penetration theory of Higbie [17].

In comparison with analytical calculations and simplifications, the numerical approach can take into the account the complicated mixing patterns and geometries. However, there are challenges as to mimic the continuous picture like moving with bulk velocity $U = U_{\text{gas}} + U_{\text{liq}}$ reacting medium as it is seen in experiments. Thus, the questions indicated in Section 1, as the choice of the characteristic concentration, the choice of boundary conditions, arise. Next section gives more details about numerical simulations.

2.3 Numerical simulations

Ideally one needs to mimic the continuous picture as it is seen in experiments. Thus, mass transfer simulations for a number of unit cells is needed. As it was indicated above, there are two approaches towards it - either to simulate the bubble train and then to measure concentration along the pipe, Eq. 9, or to transfer to the reference frame moving with the bulk velocity U and conduct

same measurements. However, both methods do require a tracking of moving bubbles which is complicated from the numerical point of view. Therefore, one needs to come up with simple smaller domain calculations of the mass transfer coefficient, which mimic the continuous picture with infinite numbers of the bubbles closely.

To avoid complications with moving grids, our approach is to simulate mass transfer in the reference frame moving with the bubble. Therefore, one needs to examine Eq. 9 more closely.

We perform simulations in the frame moving with the bubble (velocity U_{bubble}), that the bubble position stands steady. The bubble velocity U_{bubble} is different from the bulk velocity $U = U_{\text{gas}} + U_{\text{liq}}$. In this case one needs to perform a coordinate x variable change:

$$\begin{aligned} x(t) &= U_{\text{bubble}} t \\ \overline{C(x)} &= C^* \Big(1 - \exp\big(-k_L\, a \frac{x}{U_{\text{gas}} + U_{\text{liq}}}\big)\Big) \\ \langle C(t) \rangle &= C^* \Big(1 - \exp\big(-k_L\, a\, t \frac{U_{\text{bubble}}}{U_{\text{gas}} + U_{\text{liq}}}\big)\Big), \end{aligned} \tag{10}$$

where $\langle C(t) \rangle$ is the characteristic concentration averaged in space, $\overline{C(x)}$ is averaged in time concentration at location x. One can have different choices of $\langle C(t) \rangle$ as the averaged in whole domain concentration or inlet/outlet averaged in space concentrations used in works [3, 4]. Therefore, one can obtain the volumetric mass transfer coefficient through the concentration averaged in space:

$$\begin{aligned} k_L\, a\, t \frac{U_{\text{bubble}}}{U_{\text{gas}} + U_{\text{liq}}} &= \ln \frac{C^*}{C^* - \langle C(t) \rangle} \\ k_L\, a \frac{L_{\text{unit}}}{U_{\text{bubble}} + U_{\text{gas}}} &= \frac{L_{\text{unit}}}{U_{\text{bubble}} t} \ln \frac{C^*}{C^* - \langle C(t) \rangle}, \end{aligned} \tag{11}$$

where the parameter $k_L\, a \frac{L_{\text{unit}}}{U_{\text{gas}} + U_{\text{liq}}}$ is non-dimensional. One can also measure the volumetric mass transfer coefficient from concentrations given at times t_1 and t_2:

$$k_L\, a \frac{L_{\text{unit}}}{U_{\text{bubble}} + U_{\text{gas}}} = \frac{L_{\text{unit}}}{U_{\text{bubble}} (t_2 - t_1)} \ln \frac{C^* - \langle C(t_1) \rangle}{C^* - \langle C(t_2) \rangle}. \tag{12}$$

Expressions (10) and (12) are cornerstones of the present work. The main questions arisen in the present work are to define the characteristic concentration $\langle C(t) \rangle$ and boundary conditions to calculate a proper volumetric mass transfer coefficient $k_L\, a$.

Four possible scenarios of numerical simulations are examined in this work:

1. One unit cell is simulated with periodic boundary conditions, see Fig. 3. Thus, no tracer leaves a domain like for the plug flow. Though easier to implement, it rises certain criticism about the inlet concentration to be equal to the outlet concentration. As it was discussed, in experiments there is the concentration difference between the inlet and the outlet.

The volumetric mass transfer coefficient is calculated by Eq. 11. The characteristic concentration $\langle C(t) \rangle$ required for the volumetric mass transfer coefficient, Eq. 11, is taken as the average concentration in the domain:

$$C(t) = \frac{\int_{liquid} C \mathrm{d}V}{\int \mathrm{d}V}. \tag{13}$$

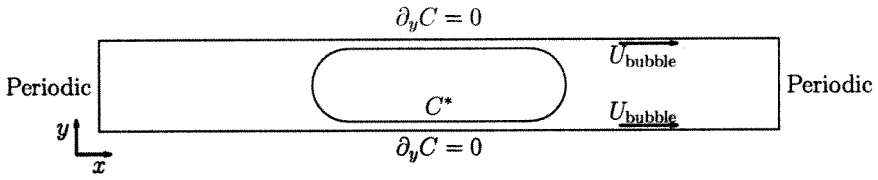

Figure 3: The two-dimensional benchmarks for the the mass transfer coefficient (bottom) for the bubble located near the entrance (top) and at the middle of the domain (bottom).

2. The second approach is to apply periodic boundary conditions as in the first case but the characteristic concentration is taken as the inlet/outlet concentration [3]:

$$\begin{aligned} \langle C_{\text{inlet}}(t) \rangle &= \frac{\int U(y) C(0, y, t) \mathrm{d}y}{\int U(0, y) \mathrm{d}y} \\ \langle C_{\text{outlet}}(t) \rangle &= \frac{\int U(y) C(L_{\text{unit}}, y, t) \mathrm{d}y}{\int U(L_{\text{unit}}, y) \mathrm{d}y} \\ C_{\text{inlet}}(\boldsymbol{x}, t) &= C_{\text{outlet}}(\boldsymbol{x}, t), \text{ due to periodicity.} \end{aligned} \tag{14}$$

Therefore, the assumptions of this approach is that the difference between inlet and outlet is not considerably large and the tracer is well mixed in the slug. Thus, the inlet or outlet concentrations equal to the average concentration.

3. The approach of van Baten and Krishna [3] is examined. Periodic boundary conditions were used. The work [3] calculates the mass transfer coefficient as the gain of the mass in the system divided by the concentration difference multiplied on the surface area:

$$k_L a = \frac{\dot{m}}{P \Delta C} \frac{P}{V} = \frac{\dot{m}}{V(C^* - \langle C(t) \rangle)}, \tag{15}$$

where mass difference in the domain can be calculated as:

$$\dot{m} = \frac{m_2 - m_1}{t_2 - t_1} = \frac{\int_{liq} C(\boldsymbol{x}, t_2) \mathrm{d}V - \int_{liq} C(\boldsymbol{x}, t_1) \mathrm{d}\boldsymbol{x}}{t_2 - t_1}. \tag{16}$$

In the approach of van Baten and Krishna the inlet and outlet concentrations were taken as the characteristic concentration $\langle C(t) \rangle$.

4. The last approach to be examined in this paper is the simulation of a few unit cells, see Fig. 4. This situation corresponds to the simulation of the bubble train head, after injecting to the pipe and travelling along the pipe. One can see that this situation corresponds most to the experimental picture. By simulation of a certain number of the bubble train head, the influence of the boundaries can be diminished. In this case, there is no ambiguity in the choice of the characteristic concentration. The average concentration of any unit cell far away from boundaries will be governed by Eq. 12. This simulation statement is of most correspondence to experiments and should give right answer. However, one of the disadvantages is to simulate a certain number of unit cells (1 to 10 in this case), thus increasing a computational burden.

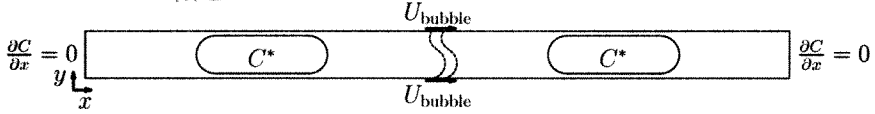

Figure 4: Benchmark for a lot of units.

One can notice that all examined cases are extreme cases of one equation:

$$k_L\, a = \frac{\dot{m} - \int C_{\text{outlet}}(t) u(L_{\text{unit}}, y) \mathrm{d}y + \int C_{\text{inlet}}(t) u(0, y) \mathrm{d}y}{V \Delta C}, \qquad (17)$$

where $\Delta C = C^* - \langle C(t) \rangle$ with $\langle C(t) \rangle$ to be the average concentration in whole liquid domain, $\dot{m}$ is the mass gain in the domain, $\int C_{\text{inlet}} u(0, y) \mathrm{d}y$ and $\int C_{\text{outlet}} u(L_{\text{unit}}, y) \mathrm{d}y$ are inlet/outlet mass fluxes. Eq. 17 describes the mass balance: whatever was generated by the bubble surface equals to the mass domain change minus whatever left domain plus whatever entered domain.

Periodic boundary condition is the extreme limiting case of Eq. 17:

$$\int C_{\text{outlet}}(t) u(L_{\text{unit}}, y) \mathrm{d}y = \int C_{\text{inlet}}(t) u(0, y) \mathrm{d}y.$$

Then the mass change in the domain is only because of the generating bubble surface. However, to calculate the mass transfer coefficient one needs to have characteristic concentration $\langle C(t) \rangle$ and mass gain $\dot{m}$ which do require the storage of time and space information.

Another limiting case (will be shown later) is hydrodynamic pattern change $Ca > 0.7$. The mass accumulation rate equals zero in this case, $\dot{m} = 0$. One can use only spatial information to calculate the mass transfer coefficient, i.e. $\int C_{\text{inlet}}(t) u(0, y) \mathrm{d}y$ and $\int C_{\text{outlet}}(t) u(L_{\text{unit}}, y) \mathrm{d}y$ require only space information.

Before we examine all the test cases above, the lattice Boltzmann mass transfer benchmarks will be presented.

3 Validation

As it was discussed analytical correlations for the mass transfer coefficient are derived as two separate contributions: the mass transfer from two circumferences and the mass transfer from the film. We will examine these problems closely with the help of the lattice Boltzmann method and compare them against analytical solutions. The next sections will give a short introduction on the lattice Boltzmann method and present a few benchmarks.

3.1 TRT $D2Q9$ model

The lattice Boltzmann equation (LBE) operates on a square/cubic grid representing the physical domain. It utilizes probability distribution functions (also known as particle populations) containing information about macroscopic variables, such as fluid density and momentum. LBE consists of two parts: a local collision step, and a propagation step which transports information from one node to another along some directions specified by the discrete velocity set. The LBE is typically implemented as follows:

$$\begin{aligned} f_i^*(\boldsymbol{x},t) &= f_i(\boldsymbol{x},t) - \omega\big(f_i(\boldsymbol{x},t) - eq_i(\boldsymbol{x},t)\big), && \text{collision step} \\ f_i(\boldsymbol{x}+\boldsymbol{c_i},t+1) &= f_i^*(\boldsymbol{x},t), && \text{propagation step,} \end{aligned} \tag{18}$$

where f_i is the probability distribution function in the direction $\boldsymbol{c_i}$, f_i^{eq} is the equilibrium probability distribution function, ω is the relaxation parameter. Collision operator, $-\omega(f_i - f_i^{eq})$ is so-called BGK collision operator [35]. However, the approach to be used here is the TRT (two-relaxation-times) collision operator [31, 33]. In comparison with the widely used BGK collision operator, TRT collision operator has better accuracy for diffusion and convection fluxes, and larger range of parameters where the LBM scheme is stable.

The TRT collision operator [36] decomposes the populations and the equilibrium distribution into the symmetric and antisymmetric parts:

$$f_i^{\pm} = \frac{f_i \pm f_{\bar{i}}}{2}\,,\quad eq_i{}^{\pm} = \frac{eq_i \pm eq_{\bar{i}}}{2}\,, \tag{19}$$

where $\bar{i}$ is the opposite direction to the i-th direction. The collision is performed with two independent relaxation rates for symmetric and antisymmetric modes:

$$\begin{aligned} f_i^*(\boldsymbol{x},t) &= f_i(\boldsymbol{x},t) - \omega_+(f_i^+ - eq_i^+) - \omega_-(f_i^- - eq_i^-) \\ f_i(\boldsymbol{x}+\boldsymbol{c_i},t+1) &= f_i^*(\boldsymbol{x},t). \end{aligned} \tag{20}$$

Note that the BGK collision operator is the particular subclass of the TRT relaxation operator with $\omega_+ = \omega_-$. In comparison with the BGK collision operator, the TRT collision operator has the additional degree of freedom. Thus, the TRT operator introduces the free parameter $\Lambda = \left(\frac{1}{\omega_+} - \frac{1}{2}\right)\left(\frac{1}{\omega_-} - \frac{1}{2}\right)$. This free parameter controls the effective location of the bounce-back walls [37], second-order accuracy of boundary [36] and interface schemes [38], spatial

accuracy [39, 40], consistency [41] and, to some extent, stability [40, 42, 43]. In particular, $\Lambda = \frac{1}{4}$ achieves the optimal stability for the linear advection-diffusion isotropic equation [42].

The parameters ω_+, ω_- and eq_i fully define the lattice Boltzmann procedure. The two-dimensional, nine velocities LBM $D2Q9$ we used in this work is defined on the set of lattice velocities with coordinates:

$$\begin{aligned} c_{ix} &= \{0, 1, 0, -1, 0, 1, -1, -1, 1\}, \text{ for } i = 0 \ldots 8 \\ c_{iy} &= \{0, 0, 1, 0, -1, 1, 1, -1, -1\}, \text{ for } i = 0 \ldots 8 \,. \end{aligned} \tag{21}$$

The equilibrium functions for $D2Q9$ TRT model are represented as [42]:

$$\begin{aligned} eq_i^{+} &= eq_i^{(m)} + g^{(u)} eq_i^{(u)} \\ eq_i^{(m)} &= t_i^{(m)} c_e + eq_i^{(a)} \\ eq_i^{(u)} &= t_i^{(u)} \frac{u_x^2 + u_y^2}{2} + \frac{u_x^2 - u_y^2}{4} p_i^{(xx)} + g_{xy}^{(u)} \frac{u_x u_y}{4} p_i^{xy} \\ eq_i^{(a)} &= \frac{K_{xx} - K_{yy}}{4} p_i^{xx} + \frac{K_{xy}}{4} p_i^{(xy)}, \end{aligned} \tag{22}$$

where $K_{xx,yy,xy}$ are proportional to components of the diffusion tensor, $c_e = \frac{K_{xx}+K_{yy}}{2}$, parameters $g^{(u)}$ and g_{xy}^{u} are either zero or one (see below), the tensor $p_i^{(xx)} = c_{ix}^2 - c_{iy}^2$, the tensor $p_i^{(xy)} = c_{ix} c_{iy}$, the weights $t_i^{(u,m,a)}$ can be chosen based on stability criteria. The most stable set of weights, so called "hydrodynamic" weights, was chosen:

$$t_i^{(u)} = t_i^{(m)} = t_i^{(a)} = \left\{0, \frac{1}{3}, \frac{1}{3}, \frac{1}{3}, \frac{1}{3}, \frac{1}{12}, \frac{1}{12}, \frac{1}{12}, \frac{1}{12}\right\} \tag{23}$$

It can be shown through the Chapman-Enskog procedure [44], that the simple update rule with the equilibrium function presented above restores the anisotropic advection-diffusion equation:

$$\partial_t C + \partial_\alpha C u_\alpha = \partial_{\alpha\beta} D_{\alpha\beta} C, \tag{24}$$

where $D_{\alpha\beta} = \left(\frac{1}{\omega_-} - \frac{1}{2}\right) K_{\alpha\beta}$ with the following diffusion tensor:

$$D_{\alpha\beta} = \begin{pmatrix} D_{xx} + \left(\frac{1}{\omega_-} - \frac{1}{2}\right)(g^{(u)} - 1) u_x^2 & D_{xy} + \left(\frac{1}{\omega_-} - \frac{1}{2}\right)(g_{xy}^{(u)} - 1) u_x u_y \\ D_{xy} + \left(\frac{1}{\omega_-} - \frac{1}{2}\right)(g_{xy}^{(u)} - 1) u_x u_y & D_{yy} + \left(\frac{1}{\omega_-} - \frac{1}{2}\right)(g^{(u)} - 1) u_y^2. \end{pmatrix} \tag{25}$$

We want to resolve the isotropic advection-diffusion equation, $D = D_{xx} = D_{yy}$ or $K = K_{xx} = K_{yy}$, with the non-diagonal diffusion tensor components to be zero $D_{xy} = 0$. In comparison with the $D2Q5$ model, with the $D2Q9$ it is possible to cancel the numerical diffusion by the proper choice of the equilibrium functions, i.e. $g_{xy}^{(u)} = g^{(u)} = 1$. The particular choice of parameters used in simulations is $c_e = \frac{1}{3}$, $\Lambda = \frac{1}{4}$. Thus, the diffusion coefficient D is matched

through ω_-, i.e. $D = c_e\left(\frac{1}{\omega_-} - \frac{1}{2}\right) = \frac{1}{3}(\frac{1}{\omega_-} - \frac{1}{2})$. The relaxation parameter ω_+ can be found through Λ. For particular choice $\Lambda = \frac{1}{4}$ (the optimal stability parameter), ω_+ can be found easily as $\omega_+ = 2 - \omega_-$.

Boundary conditions for the mass transfer used in this work are all of Dirichlet type. We validated two types of boundary conditions: Inamuro boundary conditions [34] and pressure anti bounce-back boundary conditions [37]. However, the simulation results presented in this work are only pressure anti bounce-back due to its simplicity to handle any complicated type of boundary:

$$f^*_{B,i} = -f^*_{F,\bar{i}} + 2eq^+(C^*, \boldsymbol{u}), \tag{26}$$

where C^* is the concentration to be imposed at the surface, $\boldsymbol{u}$ is the surface velocity, i is the direction number pointing to the domain (unknown) located at the boundary surface B, $\bar{i}$ is the direction number opposite to i and is located at the fluid F specifically that B is located at the location $F + \boldsymbol{c_i}$.

Note that the parameters of the lattice Boltzmann scheme are connected with physical parameters only through non-dimensional numbers governing the physics of the problem. In our case, this number is the Peclet number, $Pe = \frac{U_{\text{bubble}}L}{D}$. Therefore, one can substitute any quantity, i.e. U_{bubble} in the lattice Boltzmann units as soon as the Peclet number is matched in physical space and numerical simulations. This fact that U_{bubble} can be chosen arbitrarily is extremely useful in the context of numerical simulations, since it can increase the time step, or decrease the computational demand by order of magnitude to obtain meaningful results. This point will be used in simulations and covered later.

Next section will cover LBM benchmarks that resemble the mass transfer problem from a bubble, as mass transfer from the film and circumferences.

3.2 The radial case

The case to be examined is the mass transfer from the stair-case boundary forming a circle. It can be prescribed by the following system of equations:

$$\begin{aligned} \partial_t C(r,t) &= \frac{1}{r}\partial_r r \partial_r C(r,t) \\ C(a,t) &= C_0,\ C(r,0) = C_{init} \end{aligned} \tag{27}$$

The solution is represented as [45]:

$$\frac{C(r,t) - C_0}{C_{init} - C_0} = \sum_{n=1}^{\infty} \frac{2}{\mu_n J_1(\mu_n)} \exp\left(-\mu_n^2 \frac{Dt}{a^2}\right) J_0(\mu_n \frac{r}{a}), \tag{28}$$

where μ_n is the n-th zero root of the 0th order Bessel polynomial $J_0(\mu_n) = 0$. Some of the corresponding roots are as follows: $\mu_1 = 2.4048, \mu_2 = 5.5201, \mu_3 = 8.6537$, $\mu_4 = 11.7915, \mu_5 = 14.9309$. By taking initial concentration to be 0, one

can obtain the following solution:

$$C(r,t) = C_0\left(1 - \sum_{n=1}^{\infty} \frac{2}{\mu_n J_1(\mu_n)} \exp\left(-\mu_n^2 \frac{Dt}{a^2}\right) J_0(\mu_n \frac{r}{a})\right). \qquad (29)$$

The solution depends only on the non-dimensional time: $\tau = \frac{Dt}{a^2}$. The domain size was 129×129 with the circle radius $a = 40$ units. Some examples for different diffusion coefficients are presented in Fig.5.

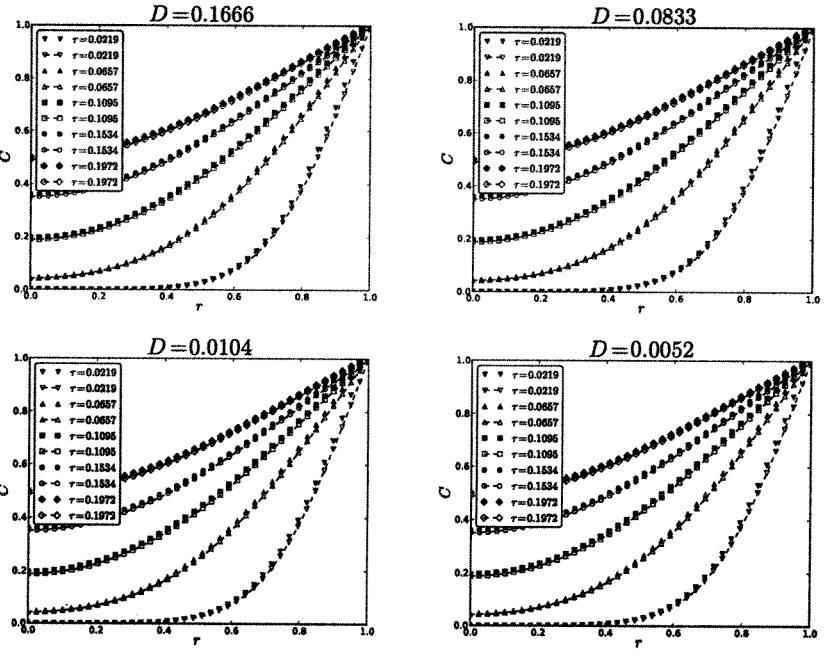

Figure 5: Profiles for different diffusion parameters varied with ω_-. One can see that the diffusion from curved boundaries is captured accurately . r is the distance from the center.

3.3 Parabolic velocity profile with the velocity zero gradient at the wall

The problem is defined in terms of PDE as follows:

$$\begin{aligned} &\frac{\partial C}{\partial x}U(y) = D\frac{\partial^2 C}{\partial y^2} \\ &C(0,y) = C_0,\ C(x,0) = C^*,\ \frac{\partial C}{\partial y}(x,\delta) = 0 \\ &U(y) = U_0\Big(\frac{y}{\delta}\Big)^2. \end{aligned} \tag{30}$$

The procedure to solve this PDE is presented in Appendix A:

$$\begin{aligned} C(x,y) &= C^* + \sum_m C_m \sqrt{\frac{y}{\delta}} J_{\frac{1}{4}}\Big(\frac{m^2}{2}\frac{y^2}{\delta^2}\Big)\exp\Big(-\frac{m^4}{Pe}\frac{x}{\delta}\Big) \\ C_m &= (C_0 - C^*)\frac{\int_{\xi=0}^1 \xi^{5/2} J_{\frac{1}{4}}\Big(\frac{m^2\xi^2}{2}\Big)\mathrm{d}\xi}{\int_{\xi=0}^1 \xi^3 J^2_{\frac{1}{4}}\Big(\frac{m^2\xi^2}{2}\Big)\mathrm{d}\xi} \end{aligned} \tag{31}$$

Fig. 6 shows the steady-state contours comparison between the analytical solution and the simulation with the anti bounce-back boundary conditions used to impose constant concentrations at the wall $C^* = 1$ and the inlet $C_0 = 0$. The simulation grid is 80×1600. Parameter $\omega_- = 1.8$ implies the diffusion coefficient to be $D = \frac{1}{3}\Big(\frac{1}{\omega} - \frac{1}{2}\Big) = 0.0185$.

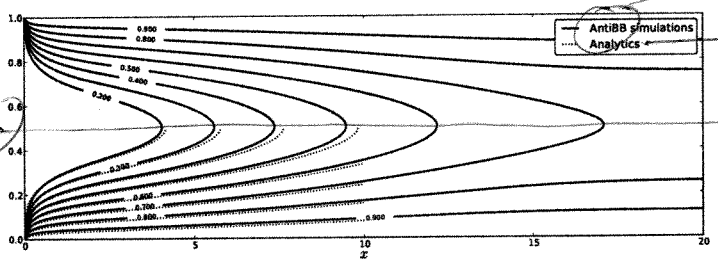

Figure 6: Concentration contour levels comparison between the analytical solution, Eq. 31, and simulation for the diffusion coefficient $D = 0.0185$. Simulation was performed on the grid size of 80×1600. The constant concentration is imposed with the anti bounce-back conditions, Eq. 26. Coordinate x and y are non-dimensionalized on the height of the channel. $\delta = H/2$ is the half of the channel height.

3.4 Poiseulle velocity parabolic profile

The problem we want to address can be formulated through the following PDE:

$$\begin{aligned} &\frac{\partial C}{\partial x}U(y) = D\frac{\partial^2 C}{\partial y^2} \\ &C(0,y) = 0,\ C(x,\pm\delta) = C^*,\ \frac{\partial C}{\partial y}(x,0) = 0 \\ &U(y) = U_0\Big(1 - \big(\frac{y}{\delta}\big)^2\Big) \end{aligned} \tag{32}$$

The procedure to solve this problem is presented in Appendix B which yields the final solution as:

$$C = C^* - C^* \sum_{m=0} C_m e^{-m^4 \frac{x}{\delta} \frac{1}{Pe}} e^{-m^2 y^2/(2\delta^2)}\, {}_1F_1\Big(-\frac{m^2}{4} + \frac{1}{4}, \frac{1}{2}, m^2\frac{y^2}{\delta^2}\Big), \tag{33}$$

where coefficients C_m are taken from Eq. 62. The comparison between contours of analytical and simulation results is presented in Fig. 7. Parameters were taken same as in the previous case: the diffusion $D = 0.0185$, the grid dimension is 80×1600.

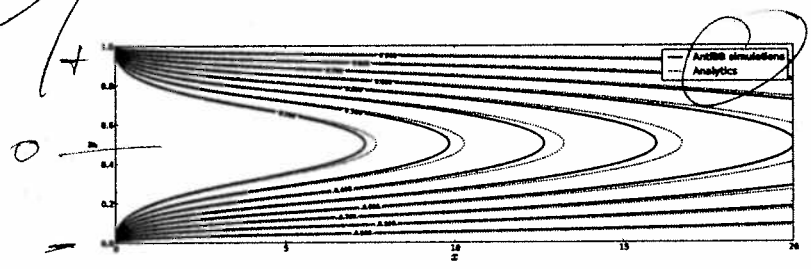

Figure 7: Comparison between the analytical concentration contours and simulations with pressure anti bounce-back conditions, Eq. 26. The parameters were taken as $D = 0.0185$ and grid 80×1600.

After the LBM is validated against the benchmarks relevant for the flow around bubbles, one can examine the cases mentioned in Section 2.3 to calculate the volumetric mass transfer coefficient.

4 Numerical approach

The multiphase code was utilized to obtain the flow patterns and bubble shapes for different capillary numbers [18]. Five particular cases were chosen to be examined, their results are summarized in Table 1. Note that velocities in Table 1 are small. It means that to match large Peclet numbers, $Pe = \frac{U_{bubble}L}{D}$, usually used in experiments, one needs to decrease the diffusion coefficient $D =$

Ca	Re	U_{bubble}	δ	ε_{gas}	U_{liq}	U_{gas}	L_{bubble}	L_{slug}
0.097	1.656	0.0055	0.092	0.30	0.0046	0.0016	5.79	9.21
0.254	4.318	0.0143	0.132	0.28	0.0108	0.0041	6.12	8.88
0.526	8.938	0.0297	0.157	0.27	0.0209	0.0080	6.19	8.81
0.750	12.744	0.0424	0.167	0.25	0.0293	0.0107	5.96	9.04
1.040	17.665	0.0588	0.177	0.22	0.0397	0.0135	5.59	9.41

Table 1: Sample results with the binary liquid lattice Boltzmann model [18]. The following notations are used: the capillary number $Ca = \frac{U_{\text{bubble}} L}{\rho \nu_{\text{liq}}}$, δ is the non-dimensional film thickness, U_{liq} is the superficial liquid velocity, U_{gas} is the superficial gas velocity. The simulation sketch is presented in Fig. 1.

$\frac{1}{3}\left(\frac{1}{\omega_-} - \frac{1}{2}\right)$. Thus, parameter $\omega_- \approx 0.5$. However, for such parameters ω_- the stability of the lattice Boltzmann method drastically decreases [43]. On the other hand, one iteration in the lattice Boltzmann system corresponds to the time step in the physical domain $\Delta t = U_{\text{bubble,LB}} \frac{\Delta x}{U_{\text{bubble,phys}}}$. One iteration time is proportional to the velocity U_{LB} and the typical number of simulation steps to obtain the steady-state mass transfer coefficient for $Ca < 0.2$ is of the order of a few millions. Therefore, it is desirable to increase velocity U_{LB} while keeping the Peclet number the same. If one increases velocity, then ω_- increases as well. Thus, the increase of the velocity impacts positively on stability of the LBM as ω_- is not close to its stability limit 0.5.

Given all the considerations above, mass transfer simulations are performed as:

Flow field Given the capillary number Ca, one needs to obtain hydrodynamic fields around the bubble using the multiphase binary liquid lattice Boltzmann model according to work [18]. Periodic boundary conditions are used. The grid used in this work is 202×3000 which corresponds to the fluid domain of size 200×3000. The grid resolution is taken to ensure grid independency of results [18]. Note that we do not approximate bubble shapes by correlations, but we directly resolve them by using the multiphase solver.

Bubble reference frame Once the hydrodynamics is resolved, the mass transfer simulations are conducted in the reference frame moving with the bubble. Then the bubble stands still and the flow is happening around the bubble. We impose a steady concentration on the surface of the bubble with the anti bounce-back condition, Eq. 26.

Velocity improvement One can scale the velocity to perform faster simulations. However, before doing it one needs to improve velocity. This issue arises because of the multiphase model used in simulations. The binary liquid lattice Boltzmann model is the diffusive interface model. Thus, the transition between gas and liquid is the continuous function. We obtain the bubble shape according to the phase indicator ϕ as used in [18], say

$\phi \leq 0$. The velocity of the bubble is calculated as the bubble tip velocity. Because of the square grid, the shape of the bubble is determined within accuracy of one grid node. Thus, there is the error in determination of the bubble velocity. Though these errors are small, however there is a small non-zero velocity component pointing to the bubble in some places, see Fig. 8 in [18] where some streamlines are penetrating a bubble surface at left. This small velocity is amplified upon the velocity scaling and is inconsistent with the advection-diffusion equation leading to the instability after many iterations.

Thus, before performing the mass transfer simulations one additional single phase hydrodynamic simulation is performed. An additional free-surface solver was developed in order to obtain velocity field consistency with the advection-diffusion equation. We take results from the multiphase simulations, extract a bubble shape using the phase indicator $\phi \leq 0$, approximate the bubble shape by the stair-case line. Then, the obtained bubble velocity is imposed on walls. This corresponds to conducting simulation in the reference frame moving with the bubble. In addition, the free-slip boundary condition on the bubble surface is imposed. Appendix C covers the simple free-slip boundary conditions implementation drastically improving velocity patterns. The system is iterated until a steady state is reached. Note, that these type of simulations are much faster than original multiphase simulations. As the output all the non-zero velocity components perpendicular to the bubble surface are completely eliminated. We compared original multiphase simulations with one-component free-slip simulations. All quantities as superficial slug and liquid velocities are within 3% for the capillary number in the range $0.05 \leq Ca \leq 1.0$. This simulation helps to make mass transfer simulations stable and faster.One can see in Fig. 19 two streamlines profiles for $Ca = 0.097$ and $Ca = 1.040$.

Mass transfer After improved velocity profiles are obtained one can perform any mass transfer simulations with different boundary conditions as covered in Section 2.3. For this purpose one needs to match the Peclet number Pe taken from experiments. Note that we specifically separated the hydrodynamic problem from the mass transfer problem.

5 Results

This section covers simulation results. We first examine the possibility to increase the fluid velocity while keeping the Peclet number the same. After the periodic boundary conditions for 5 capillary number cases will be presented. Finally, we will examine many cells simulations for two representative cases velocity patterns, as $Ca = 0.0907$ and $Ca = 1.04$ (see Fig. 8).

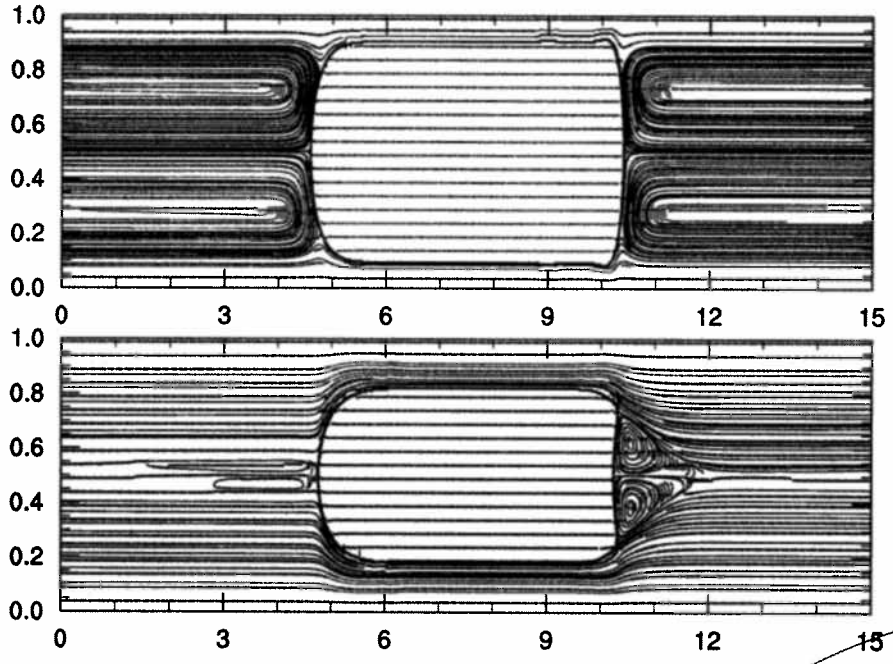

Figure 8: The streamlines patterns produced by the free-surface solver with simplistic approximation of the free-slip bubble surface, see Appendix C. Two completely different velocity patterns are covered, $Ca = 0.097$ (top) and $Ca = 1.040$ (bottom).

5.1 Keeping the Peclet number

This section addresses the simulations performance. The ultimate goal is to increase velocity magnitude significantly while keeping dimensionless parameters the same to speed up simulations. This is especially important to be able to simulate a few unit cells simulations. For example, ten unit cells simulations require a grid of 30000×202 nodes. As it was discussed above, only the Peclet number governs the advection-diffusion equation. In the lattice Boltzmann system it is represented as:

$$Pe = \frac{U_{\text{bubble}} N_y}{D}. \tag{34}$$

As far as we want to increase velocity, one needs to increase the diffusion coefficient as well. The runs were made with velocities $2, 4, 6, 8, 10, 15, 20, 40$ times larger than original velocities. The velocities and its corresponding capillary numbers are presented in Table 2. Periodic boundary conditions were used and mass transfer coefficient was calculated according to Eq. 3. Table 2 shows that the velocity limit for periodic boundary conditions is 0.1. It gives us the preliminary idea to what extent one can scale periodic mass transfer simulations. The

Scale	U_{bubble}	ω_-	Time Iterations	C_{aver}
		$Ca = 0.097, Pe = 1313$		
2	0.011	1.98	400000	0.318
4	0.023	1.96	200000	0.319
8	0.044	1.92	100000	0.320
10	0.055	1.90	80000	0.321
20	0.11	1.81	40000	0.324
40	0.22	1.66	20000	0.328
		$Ca = 0.254, Pe = 3414$		
2	0.0286	1.98	800000	0.6533
4	0.0572	1.96	400000	0.6591
8	0.1144	1.92	200000	0.6692
10	0.1430	1.90	160000	0.6734
20	0.2860	1.81	80000	0.6894
		$Ca = 0.526, Pe = 7092$		
2	0.0594	1.98	200000	0.3271
4	0.1188	1.96	100000	0.3315
		$Ca = 0.750, Pe = 10125$		
2	0.0848	1.98	200000	0.3489
		$Ca = 1.040, Pe = 14041$		
2	0.1176	1.98	200000	0.3675

Table 2: This table presents the achievable stable velocity U_{bubble} when one scales velocity. One iteration in the lattice Boltzmann system corresponds to time difference as $\Delta t = \frac{U_{\text{bubble,LB}}}{U_{\text{bubble,phys}}} \Delta x$. Therefore the speed up of the simulation is proportional to the $U_{\text{bubble,LB}}$. Note that time iterations indicated in the table correspond to the one time moment in the physical space. One can see that scaling produces adequate results. The achievable stable velocity is around $U_{bubble} = 0.1$. Average concentrations are in the reasonable agreement. The contour profiles for all of these cases (capillary number Ca and all scales) are presented in Fig. 9.

corresponding to Table 2 concentration contour profiles for different velocity scalings are presented in Fig. 9. One can see an acceptable agreement between all of them. Note, that the speedup can be upto 10 to 40 times faster.

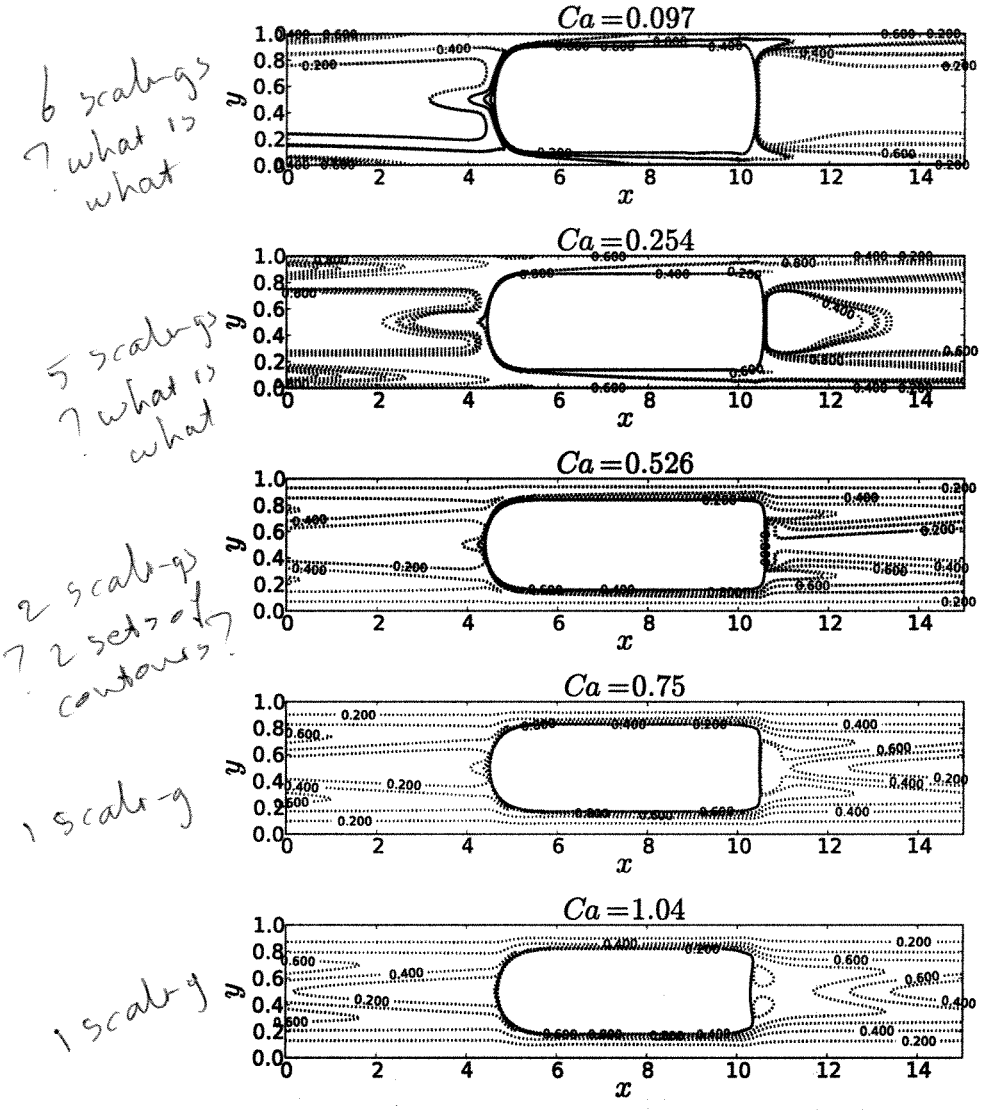

Figure 9: Concentration contour profiles for velocity scalings as identified in Table 2 (top to bottom: $Ca = 0.097, 0.254, 0.526, 0.750, 1.040$). Lines correspond to all different scales indicated in Table 2. Agreement is reasonable.

5.2 Average concentration

As indicated in Section 2.3 one can calculate the average domain concentration over the time. Eq. 11 shows how the volumetric mass transfer coefficient

depends on time, i.e. streamwise coordinate:

$$\left\{ \begin{aligned} k_L\, at \frac{U_{\text{bubble}}}{U_{\text{gas}} + U_{\text{liq}}} &= \ln \frac{C^*}{C^* - \langle C(t) \rangle} \\ k_L\, a \frac{L_{\text{unit}}}{U_{\text{gas}} + U_{\text{liq}}} &= \frac{L_{\text{unit}}}{U_{\text{bubble}} t} \ln \frac{C^*}{C^* - \langle C(t) \rangle}, \end{aligned} \right. \tag{35}$$

where $\langle C(t) \rangle$ is the average concentration in the liquid domain. Simulations for coefficient $k_L\, a \frac{U_{\text{bubble}}}{U_{\text{gas}}+U_{\text{liq}}}$ are shown in Fig. 10 for different Peclet numbers and velocity scalings indicated in Table 2. When the average concentration goes close to $C^* = 1$ then Eq. 11 gives inadequate results due to accuracy of the logarithmic function. Fig. 10 presents the volumetric mass transfer coefficient against number of iterations. However, due to scaling each simulation has a different physical time step. We scaled curves against number of cell units which tracer will pass with the given bubble velocity, i.e. $N_{\text{cell units}} = \frac{\text{scale} \cdot U_{\text{bubble}} \cdot N_{\text{iter}}}{L_{\text{unit}}}$. Fig. 11 shows the volumetric mass transfer dependency against the distance in unit cells length. One can see in Table 3 that for different Peclet numbers different time (number of unit cells) is required to achieve the steady state. For example, for larger Peclet number less number of iterations are required to achieve the steady state condition.

Overall one is guaranteed to obtain the steady state volumetric mass transfer coefficient for periodic boundaries simulations if the following conditions are fulfilled:

I Scaling is performed as $U_{max} = \text{scale} \cdot U_{\text{bubble}} \leq 0.1$.

II The larger Peclet number the less number of iterations is required. One can extrapolate data from Table 3, say L_{steady} and estimate the number of iterations to reach the steady-state as $\text{scale} \cdot U_{\text{bubble}} \cdot N_{\text{iter}} \leq L_{\text{steady}}$.

Also, Table 3 shows the achieved steady state volumetric mass transfer coefficient.

Ca	Pe	$L_{\text{steady}}/L_{\text{unit}}$	$k_L\, a \frac{L_{\text{unit}}}{U_{\text{bubble}}+U_{\text{gas}}}$
0.097	1313	7	0.21
0.254	3414	6	0.14
0.526	7092	3	0.095
0.750	10125	3	0.074
1.040	14041	2	0.0601

Table 3: The distance which a bubble propagates when the steady-state condition is achieved. One can see that increasing Peclet number helps to achieve the steady state faster.

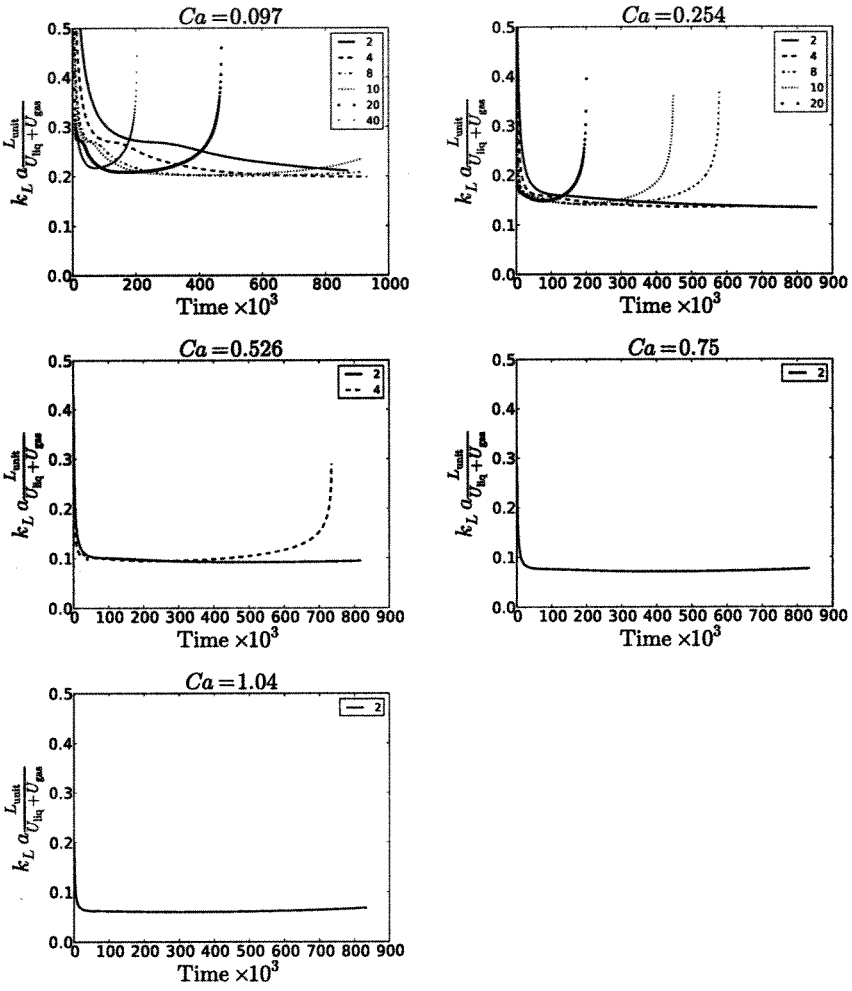

Figure 10: Calculated volumetric mass transfer coefficient for different capillaries and scales against time. One can see that all curves have the same minimum corresponding to the volumetric mass transfer coefficient. Some simulations show the volumetric mass transfer coefficient going up due to the average concentration being close to C^*. All of them show an excellent agreement. Note, that with the scaling one can reduce the amount of calculations drastically. However, one needs to be attentive because with the large velocity scaling average concentration can quickly approach C^*, thus getting an infinite volumetric mass transfer coefficient.

leave out Fig 10, only present Fig. 11

5.3 Periodic boundaries with the inlet/outlet characteristic concentration

The volumetric mass transfer coefficient was calculated using Eq. 11 with the characteristic concentration being the inlet/outlet flux averaged concentration

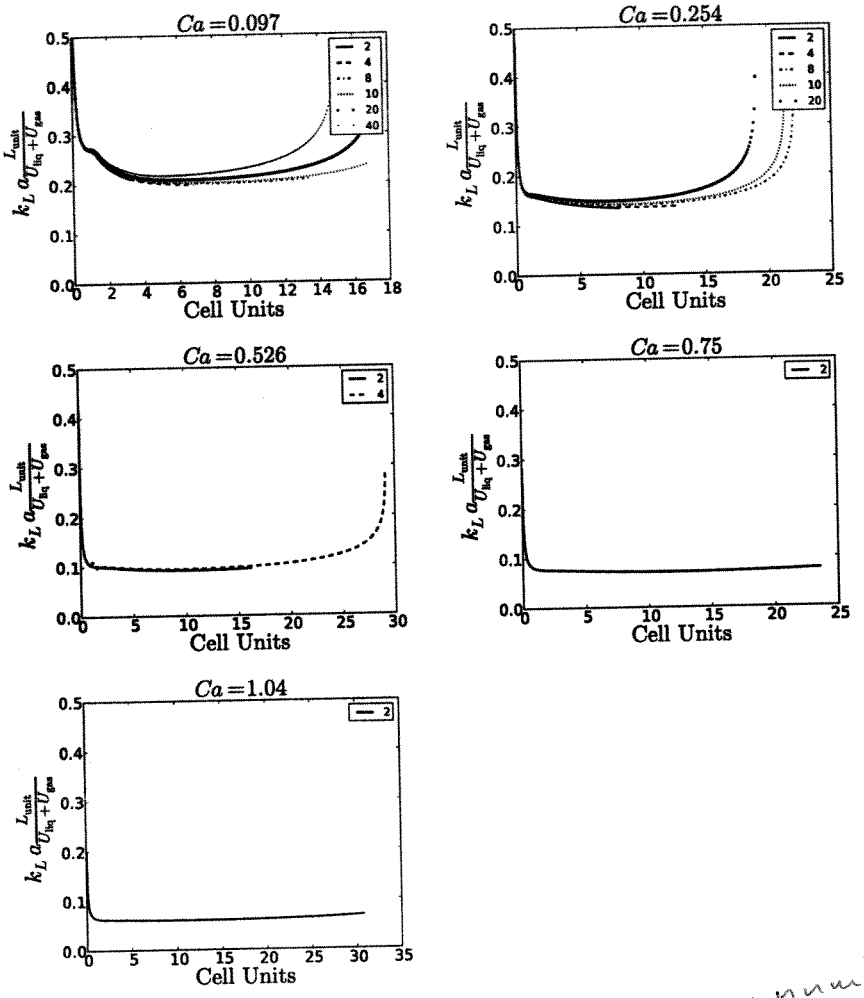

Figure 11: Volumetric mass transfer coefficient for different capillaries and scales against the bubble traveling distance in the laboratory frame. "Cell Units" axis is refered to the physical distance of how many unit cells the bubble passes until the steady state is reached. Table 3 summarizes results.

as used by van Baten and Krishna [3]. One can see in Fig. 12 the calculated volumetric mass transfer is different from the domain averaged calculated volumetric mass transfer coefficient. For example, for small capillary numbers, i.e. $Ca = 0.097, 0.254, 0.526$ the predicted values are overpredicted ($k_L\,a\frac{L_{\text{unit}}}{U_{\text{bubble}}+U_{\text{gas}}} = 0.3, 0.25, 0.1$). When the velocity pattern is changed from having vortex in front of the bubble to not having it, i.e. $Ca = 0.75, 1.04$ the calculated values are un-

derpredicted than in the previous case, i.e. $k_L\, a \frac{L_{\text{unit}}}{U_{\text{bubble}}+U_{\text{gas}}} = 0.06, 0.04$. As we will see later the domain averaged characteristic concentration produces proper results.

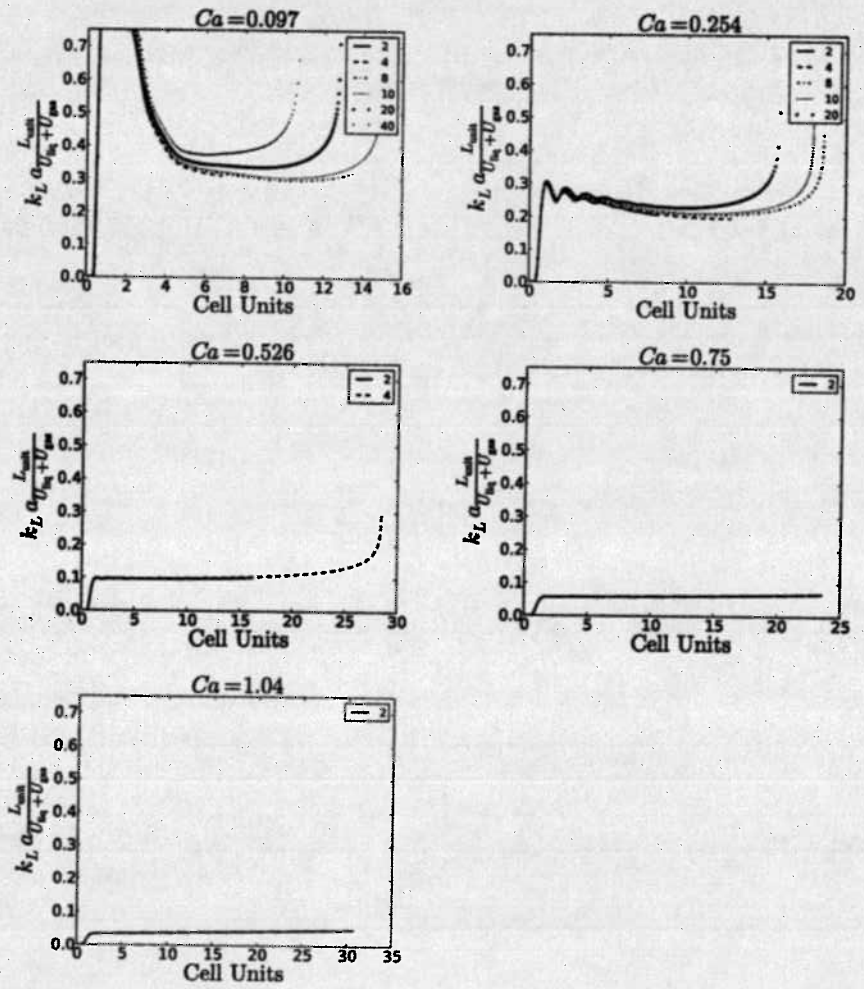

Figure 12: The volumetric mass transfer coefficient with the characteristic concentration based on the inlet/outlet flux averaged concentration as in [3]. One can see that values are either overpredicted or underpredicted than values specified in Table 3 depending on the velocity pattern.

5.4 Van Baten and Krishna formulation

The van Baten formulation, Eq. 15, is calculated as the change of mass in domain divided on the time difference. We examined two approaches: the characteristic concentration to be as the average domain simulation and as the averaged flux input/output concentration. The latter case corresponds to the work [3]. The results are presented in Fig. 13 for $Ca = 0.097$ and $Ca = 1.04$. One can see that the inlet/outlet flux averaged concentration is shown to be inconsistent. The reason that van Baten and Krishna [3] obtained the mass transfer coefficient close to the analytical estimation is that the liquid slug is well mixed that the averaged concentration is close to the inlet/outlet concentration.

However, results for the domain averaged concentration using the approach of van Baten and Krishna is close to simulation results in Section 5.2. Note that for $Ca = 0.097$ the obtained mass transfer coefficient value is a bit less than the value in Section 5.2. However, as it will be shown later the obtained volumetric mass transfer coefficient for $Ca = 0.0097$ has the same value as for the simulations of a few unit cells. Therefore this approach produces most accurate results but requires the results in time and space to calculate the mass change in time and the averaged domain characteristic concentration.

5.5 Performing a number of cell units simulations

A few unit cells simulations naturally resemble the real experiments picture. The idea here is that if one have enough number of unit cells then results of internal unit cells should be independent of boundaries and correspond to experiments. A few unit cells simulations physically correspond to the simulation of bubble train head. If boundaries are eliminated then the average domain characteristic should be changed in time according to Eq. 12. It means that there is no ambiguity to choose the characteristic concentration. The characteristic concentration is the averaged domain concentration as it is seen in experiments.

This section studies a number of the unit cells required for the volumetric mass transfer coefficient to be independent of boundaries. We chose two different velocity patterns (see Fig. 8 for $Ca = 0.097$ and $Ca = 1.04$) to perform a few number of cells simulations. For $Ca = 0.097$ we performed simulations with 4,6,8,10 number of cells, for $Ca = 1.040$ only 4,6,8 unit cells simulations. However, simulations with 10 unit cells domain length produce the same results as 8 unit cells. Thus, it won't be covered here, especially as it requires extensive computational resources (grid is 30000 × 202 nodes).

As it was discussed in the previous section we want to keep velocity around $0.05 - 0.1$ to avoid computational burden. The number of steps for mass to cross whole domain is limited from above by $1.5\frac{L_{\text{unit}}}{U_{\text{bubble}}}$, which takes into the account the bulk velocity. If U_{bubble} is taken as 0.05 then for the domain size $L_{\text{unit}} = 3000$ one can obtain the following number of iteration for mass transfer to cross the unit cell $1.5\frac{3000}{0.05} = 90000$. Therefore, 10^6 time iterations are enough for system consisting of 10 cell units. For more accurate estimations of number of time iterations depending on the Peclet number one can refer to Section 5.1.

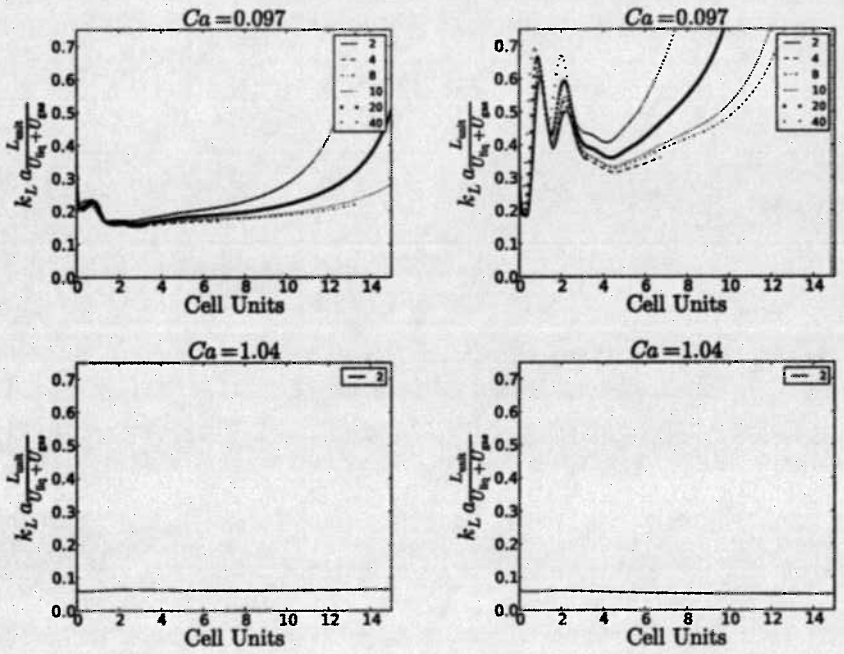

Figure 13: The van Baten and Krishna [3] formulations for $Ca = 0.097$ (top) and $Ca = 1.04$ (bottom) with the characteristic concentration being domain averaged (left) and inlet/outlet flux averaged concentration (right). One can see that van Baten and Krishna [3] formulation produces good results with the characteristic concentration being the average concentration. Moreover, the values are more close to values obtained with many cells simulations, see Fig. 15, than in comparison with periodic boundary simulations in Section 5.2. However, the characteristic concentration being inlet/outlet flux averaged concentration does not produce consistent results as in Section 5.3.

5.6 $Ca = 0.097$ results

There are two characteristics we want to track for a few unit cells simulations: the average concentration in the unit cell with time (see Eq. 12), and the accumulated mass rate in the domain adjusted with inlet/outlet fluxes (see Eq. 17). The former resembles the experimental picture: if one have enough unit cells then the averaged domain concentration should change in time according to Eq. 12:

$$k_L\, a \frac{L_{\text{unit}}}{U_{\text{gas}} + U_{\text{liq}}} = \frac{L_{\text{unit}}}{U_{\text{bubble}}(t_2 - t_1)} \ln\left(\frac{C^* - \langle C(t_1)\rangle}{C^* - \langle C(t_2)\rangle}\right) \tag{36}$$

The non-dimensional volumetric mass transfer coefficient calculated based on Eq. 36 (averaged domain concentration changes in times) is represented in Fig. 15 for different unit cells. One can see that the results are consistent with the mass flux concentration based on van Baten and Krishna formulation with the characteristic concentration being averaged domain concentration (see Section 5.4). That proves two things: the domain averaged concentration is the only choice for the characteristic concentration, and periodic boundary conditions for one unit cell produce good results.

In comparison with periodic boundary conditions Eq.17 allows to calculate the mass transfer coefficient differently. Eq. 17 can be rewritten as:

$$k_L\, a \frac{L_{\text{unit}}}{U_{\text{bubble}} + U_{\text{gas}}} = \frac{L_{\text{unit}}}{U_{\text{gas}} + U_{\text{bubble}}} \frac{V \frac{\langle C(t_2)\rangle - \langle C(t_1)\rangle}{t_2 - t_1}}{\dots}$$
$$\frac{-\int C_{\text{outlet}}(L_{\text{unit}}, y, t^*) u(L_{\text{unit}}, y)\mathrm{d}y + \int C_{\text{inlet}}(0, y, t^*) u(0, y)\mathrm{d}y}{V(C^* - \langle C(t^*)\rangle)}, \tag{37}$$

where t^* is medium time between t_1 and t_2. Fig. 14 shows average concentrations in different units and $k_L\, a \frac{L_{\text{unit}}}{U_{\text{bubble}} + U_{\text{gas}}}$ based on Eq. 37 calculated for each unit for velocity scale 10 and 6 unit cells (all velocity scales produce same results). It is shown that the volumetric mass transfer cofficient is consistent for internal segments, i.e. 3 – 5 unit cells numbers. The results for the volumetric mass transfer coefficient calculated by Eq. 17 for a few unit cells are close to the results for periodic boundary conditions in Section 5.2. The same dependencies can be found for 8 and 10 unit cells simulations but we do not present them here. As well we do not present 4 units cells simulation results which are influenced by inlet and outlet boundaries.

Though the calculation of the volumetric mass transfer coefficient is harder using Eq. 37. However, it will be shown below that this equation can be significantly simplified in case of larger capillary numbers ($Ca > 0.7$).

5.7 $Ca = 1.040$ results

The same correlations were examined for the different velocity pattern $Ca = 1.040$. A few unit cells simulations with the original Peclet number $Pe = 14041$. To improve stability we changed the original Peclet number by increasing diffusion

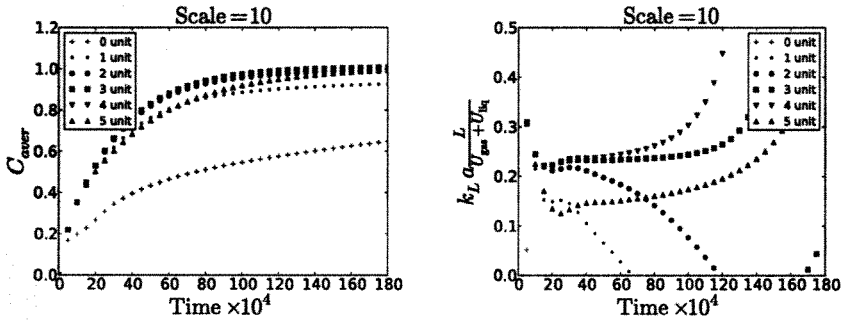

Figure 14: Average concentrations (left) and volumetric coefficients (right) for 6 units cells. The volumetric mass transfer coefficient is calculated based on Eq. 37 and accounts for inlet and outlet fluxes.

to $Pe = 2644$. The results for unit cells are the same as for $Ca = 0.097$: at least 6 unit cells are required to be simulated to avoid the influence of boundaries. Thus, only 6 unit cells results are presented in Fig. 16 which shows only the average concentration for each unit cell. One can see that the average volume concentration for each unit cell come to constant values and are not increasing with time. Thus, all the mass generated with medium is transferred through the boundaries. This is the indication that the liquid slug is not mixed. Note that the periodic boundary conditions can not show whether the liquid slug is mixed or not due to the fact that the averaged domain concentration always increases in time. Thus, the volumetric mass transfer coefficient $k_L\, a \frac{L_{\text{unit}}}{U_{\text{bubble}}+U_{\text{gas}}}$ can be calculated according to the definition, Eq. 17:

$$k_L\, a = \frac{\dot{m} - \int C_{\text{outlet}}(y) u(L_{\text{unit}}, y)\mathrm{d}y + \int C_{\text{inlet}}(y) u(L_{\text{unit}}, y)\mathrm{d}y}{V(C^* - \langle C(t)\rangle)}, \qquad (38)$$

where V is the unit cell volume. There is no accumulated mass in the domain. Thus, $\dot{m} = 0$. As periodic boundary conditions this case is another extreme limit of Eq. 17. Note that to calculate the volumetric mass transfer coefficient one needs only the spatial information and does not require the knowledge of how the averaged concentration is changed in time. This approach is the file storage saving computational approach for the Bretherton/Taylor phenomenon flow with $Ca > 0.7$ where there is no vortex in the liquid slug.

Fig. 17 (bottom) shows the volumetric mass transfer coefficient based on spatial calculations of inlet/outlet concentrations. One can see that the volumetric mass transfer coefficient is close to the calculated volumetric mass transfer coefficient using the time averaged approach and periodic boundaries one unit cells simulations presented in the same figure for comparison reasons. Note that all approaches coincide. Therefore, for certain hydrodynamic patterns ($Ca > 0.7$) one can easily convert time domain to the spatial domain calculations.

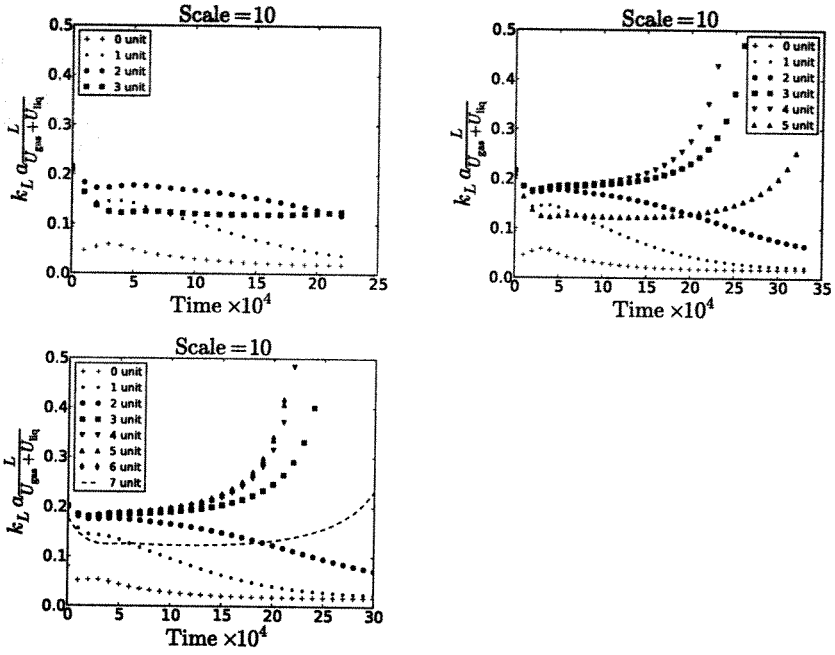

Figure 15: The non-dimensional volumetric mass transfer coefficient defined in Eq. 36 for 4 (top left),6 (top right),8 cell units (bottom). Only scale 10 is presented since all other simulations produce the same results. One can see that 4 unit cells is not enough to avoid the influence of boundaries. However, the results for 6 and 8 unit cells are consistent and show that beginning from third unit cell the results and ending with prelast cell results are consistent with periodic boundary simulations and van Baten and Krishna [3] formulations.

5.8 Experiment and Analytical correlations comparison

The goal of this paper is not to compare simulation results with the experimental correlations, but give the procedure to perform numerical simulations in the lattice Boltzmann framework. However, the small comparison is performed. Unfortunately the experiments to the best authors' knowledge measuring the mass flux for bubbles flowing between parallel plates are absent. However, one of interesting correlations for the mass transfer volumetric coefficient was

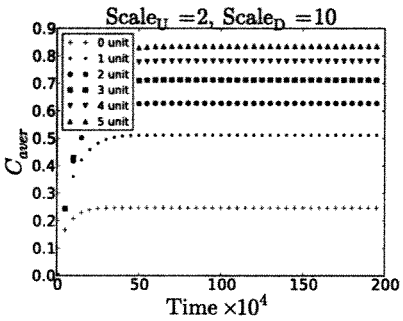

Figure 16: Results for 6 unit cells. The Peclet number equals to $Pe = 2644$. One can see that average concentrations reach certain number and stay. That means whatever was generated by medium is transferred through the outlet boundary. This is the indication that the tracer in the slug is not mixed and the volumetric mass transfer coefficient, $k_L\, a \frac{L_{\text{unit}}}{U_{\text{bubble}}+U_{\text{gas}}}$, can be calculated using the spatial approach, see Fig. 17.

presented by Yue et al. [8] for three-dimensional microchannel geometries:

$$
\begin{aligned}
k_L\, a &= \frac{2}{d_h}\Big(\frac{DU_{\text{bubble}}}{L_{\text{bubble}}+L_{\text{slug}}}\Big)^{0.5}\Big(\frac{L_{\text{bubble}}}{L_{\text{bubble}}+L_{\text{slug}}}\Big)^{0.3}\\
k_L\, a\frac{L_{\text{unit}}}{U_{\text{gas}}+U_{\text{liq}}} &= 2\frac{L_{\text{unit}}}{d_h}\Big(\frac{D}{L_{\text{unit}}(U_{\text{bubble}}+U_{\text{gas}})}\frac{U_{\text{bubble}}}{U_{\text{gas}}+U_{\text{liq}}}\Big)^{0.5}\Big(\frac{L_{\text{bubble}}}{L_{\text{bubble}}+L_{\text{slug}}}\Big)^{0.3} \propto Pe^{-\frac{1}{2}}\\
k_L\, a\frac{L_{\text{unit}}}{U_{\text{gas}}+U_{\text{liq}}} &= 2\frac{L_{\text{unit}}}{d_h}\Big(\frac{D}{L_{\text{unit}}(U_{\text{bubble}}+U_{\text{gas}})}\frac{U_{\text{bubble}}}{U_{\text{gas}}+U_{\text{liq}}}\Big)^{0.5}\Big(\frac{L_{\text{bubble}}}{L_{\text{bubble}}+L_{\text{slug}}}\Big)^{0.3} \propto Pe^{-\frac{1}{2}}
\end{aligned}
\tag{39}
$$

One can see that approximately the volumetric mass transfer correlation should be proportional to $Pe^{-0.5}$. As well one can use analytical estimations for the volumetric mass transfer coefficient calculated using the Higbie penetration theory [17]. One can derive by following works [3, 16] that the analytical expression for the flow between plates has the following form:

$$
\begin{aligned}
k_L\, a\frac{L_{\text{unit}}}{U_{\text{bubble}}+U_{\text{gas}}} = \frac{L_{\text{unit}}}{U_{\text{gas}}+U_{\text{liq}}}\Big(&4\sqrt{DU_{\text{bubble}}\pi}\frac{\sqrt{L_{\text{bubble}}-H(1-2\delta)}}{L_{\text{unit}}H}\\
&+2\sqrt{2}\sqrt{DU_{\text{bubble}}}\frac{\sqrt{H(1-2\delta)}}{L_{\text{unit}}H}\Big),
\end{aligned}
\tag{40}
$$

where H is the channel height, δ is the film thickness.

Fig. 18 shows a comparison between correlation by Yue et al. [8], analytical expression, Eq. 40, and the current simulation coefficients presented in Table 3. The coefficients are close to each other, especially given that the correlation by Yue et al. [8] is for three-dimensional cases. The fitting procedure showed that the power of the Peclet number Pe is -0.50038 which is close to -0.5.

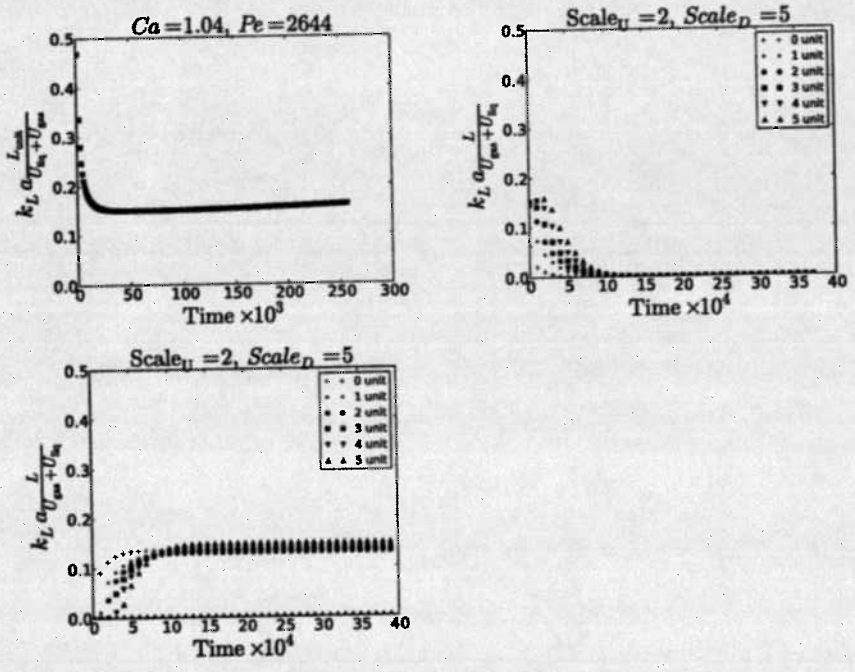

Figure 17: The periodic (top left, 1 unit cell, Eq. 12), unit cells averaged domain concentrations in time (top right, 6 unit cells, Eq. 12), and spatial location (bottom, 6 unit cells, Eq. 38) calculated volumetric mass transfer coefficients. One can see that they all coincide. However, the periodic boundary conditions based calculations produce a bit overestimated volumetric mass transfer coefficient. As well one can see that the averaged domain concentration simulations (top right) reach the steady volumetric concentrations fast and after that start decaying. It is not convenient to use them in practical cases for not mixed slug, i.e. $Ca > 0.7$.

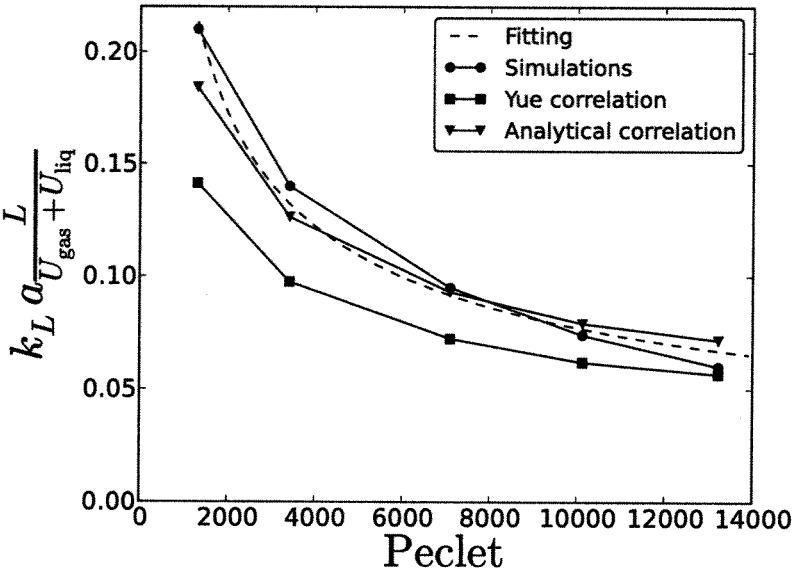

Figure 18: Comparison between the correlation by Yue et al. [8], the analytical correlation derived by following the work [16] and the mass transfer coefficient based on periodic boundary conditions. The fitting curve is proportional to $Pe^{-0.5}$ which corresponds to all correlations. As well one can see that the deviation from the analytical expression becomes larger with the Peclet number increasing the. It is because the analytical expression does not account for the velocity pattern and a bubble shape change.

6 Conclusion

This work examines a way to calculate the volumetric mass transfer coefficient in the framework of the lattice Boltzmann method. Overall, the easiest recipe is to perform periodic boundary conditions simulations and calculate the volumetric mass transfer coefficient based on the averaged domain concentration through any formulation as they produce consistent results. The best accuracy is achieved with formulations based on the mass difference or on the averaged domain concentrations taken in different times, Eq. 12. Eq. 10 gives a bit overestimated volumetric mass transfer coefficient. The original formulation of van Baten and Krishna [3] is inconsistent if one takes the inlet/outlet flux averaged concentration to be characteristic concentration. A few unit cells simulations are harder to perform, but they have indicator of how well the liquid slug is mixed. As well, for velocity patterns of $Ca \geq 0.7$ simulations with a few unit

cells allow to calculate the volumetric mass transfer coefficient only based on the spatial location, not time snapshots of domain concentration values used in all other approaches. Finally, a sample of results was compared with the experimental correlation of Yue et al. [8] and shows good agreement.

A Analytical solution for parabolic profile with zero velocity gradient at 0

The problem is defined in terms of PDE as follows:

$$\begin{aligned} &\frac{\partial C}{\partial x}U(y) = D\frac{\partial^2 C}{\partial y^2} \\ &C(0,y) = C_0,\ C(x,0) = C^*,\ \frac{\partial C}{\partial y}(x,\delta) = 0 \\ &U(y) = U_0\left(\frac{y}{\delta}\right)^2 \end{aligned} \tag{41}$$

The non-dimensional parameters are introduced:

$$\begin{aligned} &\frac{\partial C}{\partial \frac{x}{\delta}}\frac{U_0}{\delta}\left(\frac{y}{\delta}\right)^2 = \frac{D}{\delta^2}\frac{\partial^2 C}{\partial \frac{y^2}{\delta^2}} \\ &C(0,y) = C_0,\ C(x,0) = C^*,\ \frac{\partial C}{\partial y}(x,\delta) = 0 \end{aligned} \tag{42}$$

After a change of variables:

$$\begin{aligned} \zeta &= \frac{x}{\delta}\frac{D}{U_0\delta} = \frac{1}{Pe}\frac{x}{\delta} \\ \xi &= \frac{y}{\delta}, \end{aligned} \tag{43}$$

Eq. 41 with boundary conditions becomes as follows:

$$\begin{aligned} &\frac{\partial C}{\partial \zeta}\xi^2 = \frac{\partial^2 C}{\partial \xi^2} \\ &C(0,\xi) = C_0 \\ &C(\zeta,0) = C^* \\ &\frac{\partial C}{\partial \xi}(\zeta,1) = 0 \end{aligned} \tag{44}$$

Still Eq. 44 cannot be solved with the separation of variables as it requires homogenous boundary conditions. Thus, let us introduce the new variable, $\Theta = C - C^*$, which makes the system to be with homogenous boundary conditions:

$$\begin{aligned} &\frac{\partial \Theta}{\partial \zeta} = \frac{1}{\xi^2}\frac{\partial^2 \Theta}{\partial \xi^2} \\ &\Theta(0,\xi) = C_0 - C^* \\ &\Theta(\zeta,0) = 0,\ \partial_\xi \Theta(\zeta,1) = 0 \end{aligned} \tag{45}$$

This equation can be solved by separation of variables if the solutions is represented as the multiplication of two functions $\Theta(\zeta,\xi) = X(\zeta)Y(\xi)$:

$$\begin{aligned} \frac{\mathrm{d}X(\zeta)}{\mathrm{d}\zeta}Y(\xi) &= \frac{X(\zeta)}{\xi^2}\frac{\mathrm{d}^2Y(\xi)}{\mathrm{d}\xi^2} \\ \frac{1}{X(\zeta)}\frac{\mathrm{d}X(\zeta)}{\mathrm{d}\zeta} &= \frac{1}{\xi^2 Y(\xi)}\frac{\mathrm{d}^2Y(\xi)}{\mathrm{d}\xi^2} \end{aligned} \tag{46}$$

The left and right parts depend on different variables. Therefore to be equal to each other both parts shall equal to constant, say $-m^4$. Thus, the separation of the variables leads to two ODEs:

$$\begin{aligned} \frac{\mathrm{d}X(\zeta)}{\mathrm{d}\zeta} &= -m^4 X(\zeta) \\ \frac{\mathrm{d}^2Y(\xi)}{\mathrm{d}\xi^2} &+ m^4\xi^2 Y(\xi) = 0 \end{aligned}$$

The solution of the first equation is the exponential function:

$$X(\zeta) = \exp(-m^4\zeta) \tag{47}$$

The solutions of the second equation are two hypergeometric function which can be expressed through the Bessel functions [46]:

$$\begin{aligned} Y_1 &= \sqrt{\xi}J_{\frac{1}{4}}\Big(\frac{m^2\xi^2}{2}\Big) \\ Y_2 &= \sqrt{\xi}J_{-\frac{1}{4}}\Big(\frac{m^2\xi^2}{2}\Big) \\ Y_1' &= m^2\xi^{3/2}J_{-\frac{3}{4}}\Big(\frac{m^2\xi^2}{2}\Big) \\ Y_2' &= m^2\xi^{3/2}J_{\frac{3}{4}}\Big(\frac{m^2\xi^2}{2}\Big) \end{aligned} \tag{48}$$

The solution is the summation of two functions:

$$Y(x) = C_1Y_1(x) + C_2Y_2(x).$$

One can find coefficients from the boundary conditions:

$$\begin{aligned} &Y(0) = 0 = C_1Y_1(0) + C_2Y_2(0) \\ &Y_1(0) = 0,\, Y_2(0) = \frac{\sqrt{2}}{\sqrt{m}\Gamma(3/4)}C_2 = 0 \\ &Y'(1) = 0 = C_1Y_1'(1) + C_2Y_2'(1) = C_1Y_1'(1) \\ &J_{-\frac{3}{4}}\Big(\frac{m^2}{2}\Big) = 0 \end{aligned} \tag{49}$$

Therefore one needs to find zeros of $J_{-\frac{3}{4}}\Big(\frac{m^2}{2}\Big)$. To give some numerical values: $m_1 = 1.454997085$, $m_2 = 2.927133004$, $m_3 = 3.857578101$, $m_4 = 4.601777732$,

$m_5 = 5.240824067$. Therefore, the solution in a general form is represented as:

$$\Theta(\zeta,\xi) = \sum_m C_m \sqrt{\xi} J_{\frac{1}{4}}\Big(\frac{m^2\xi^2}{2}\Big) \exp(-m^4\zeta) \tag{50}$$

To find unknown coefficients C_m one needs to substitute the expression above to the initial condition:

$$\Theta(0,\xi) = C_0 - C^* = \sum_m C_m \sqrt{\xi} J_{\frac{1}{4}}\Big(\frac{m^2\xi^2}{2}\Big) \tag{51}$$

Using the Stourm-Liouville theorem one can multiply by $\xi^{5/2} J_{\frac{1}{4}}\Big(\frac{m^2\xi^2}{2}\Big)$ and integrate left and right parts of the equation:

$$\begin{aligned} &(C_0 - C^*)\int_{\xi=0}^{1} \xi^{5/2} J_{\frac{1}{4}}\Big(\frac{m^2\xi^2}{2}\Big)\mathrm{d}\xi = C_m \int_{\xi=0}^{1} \xi^3 J^2_{\frac{1}{4}}\Big(\frac{m^2\xi^2}{2}\Big)\mathrm{d}\xi \\ &C_m = (C_0 - C^*)\frac{\int_{\xi=0}^{1} \xi^{5/2} J_{\frac{1}{4}}\Big(\frac{m^2\xi^2}{2}\Big)\mathrm{d}\xi}{\int_{\xi=0}^{1} \xi^3 J^2_{\frac{1}{4}}\Big(\frac{m^2\xi^2}{2}\Big)\mathrm{d}\xi} \end{aligned} \tag{52}$$

Therefore, the overall solution is specified as:

$$\begin{aligned} &C(x,y) = C^* + \sum_m C_m \sqrt{\frac{y}{\delta}} J_{\frac{1}{4}}\Big(\frac{m^2}{2}\frac{y^2}{\delta^2}\Big) \exp\Big(-\frac{m^4}{Pe}\frac{x}{\delta}\Big) \\ &C_m = (C_0 - C^*)\frac{\int_{\xi=0}^{1} \xi^{5/2} J_{\frac{1}{4}}\Big(\frac{m^2\xi^2}{2}\Big)\mathrm{d}\xi}{\int_{\xi=0}^{1} \xi^3 J^2_{\frac{1}{4}}\Big(\frac{m^2\xi^2}{2}\Big)\mathrm{d}\xi} \end{aligned} \tag{53}$$

For the sake of completeness, we list 5 first coefficients for a case $C_0 = 0$ and $C^* = 1$: $C_1 = -1.5217$, $C_2 = -0.4933$, $C_3 = -0.3243$, $C_4 = -0.2486$, $C_5 = -0.2044$.

B The Poiseuille parabolic profile

Close to the previous example but with a different velocity profile, the benchmark can be formulated through the following PDE:

$$\begin{aligned} &\frac{\partial C}{\partial x} U(y) = D\frac{\partial^2 C}{\partial y^2} \\ &C(0,y) = 0,\ C(x,\pm\delta) = C^*,\ \frac{\partial C}{\partial y}(x,0) = 0 \\ &U(y) = U_0\Big(1 - \big(\frac{y}{\delta}\big)^2\Big) \end{aligned} \tag{54}$$

BC's
vel
profile

The same procedure can be done as in the previous case to redefine variables. After substitution the following equation can be obtained:

$$\begin{aligned} &\frac{\partial\Theta}{\partial\zeta}(1-\xi^2) = \frac{\partial^2 C}{\partial\xi^2} \\ &\Theta(\zeta,\xi) = C - C^*\,\Theta(0,\xi) = -C^*\,\Theta(0,\pm 1) = 0 \end{aligned} \tag{55}$$

After separation of variables, $\Theta(\zeta,\xi) = X(\zeta)Y(\xi)$ one can come up with two equations:

$$\begin{aligned} &\frac{\mathrm{d}X(\zeta)}{\mathrm{d}\zeta} + m^4 X(\zeta) = 0 \\ &\frac{\mathrm{d}^2 Y(\xi)}{\mathrm{d}\xi^2} + m^4(1-\xi^2)Y(\xi) = 0 \end{aligned} \tag{56}$$

The first equation has a solution:

$$X(\zeta) = \exp(-m^4\zeta) \tag{57}$$

The second equation can be simplified after substitution $\bar{\xi} = m\sqrt{2}\xi$ to the standard equation:

$$Y'' - \left(\frac{1}{4}\xi^2 + a\right)Y = 0. \tag{58}$$

The equation above has two solutions via parabolic cylinder functions or through the confluent hypergeometric function [46]:

$$\begin{aligned} Y_1 &= e^{-x^2/4}{}_1F_1\left(\frac{a}{2}+\frac{1}{4},\frac{1}{2},\frac{x^2}{2}\right) \\ Y_2 &= e^{-x^2/4}{}_1F_1\left(\frac{a}{2}+\frac{3}{4},\frac{3}{2},\frac{x^2}{2}\right) \end{aligned} \tag{59}$$

Taking symmetry conditions in the consideration by leaving only even solution, Eq. 56 has a solution as:

$$Y_m = C_m e^{-m^2x^2/2}{}_1F_1\left(-\frac{m^2}{4}+\frac{1}{4},\frac{1}{2},m^2x^2\right) \tag{60}$$

To satisfy boundary condition we need to find zeros of the hypergeometric function, i.e. ${}_1F_1\left(-\frac{m^2}{4}+\frac{1}{4},\frac{1}{2},m^2\right) = 0$. First ten eigenvalues can be found using numerical methods, as 1.2967, 2.3811,3.1093,3.6969,4.2032,4.6548,5.0662, 5.4467, 5.8023,6.1373. One needs to satisfy one more condition to obtain coefficients C_m:

$$-C^* = \sum_m C_m e^{-m^2x^2/2}{}_1F_1\left(-\frac{m^2}{4}+\frac{1}{4},\frac{1}{2},m^2x^2\right) \tag{61}$$

One can multiply both parts on $(1-x^2){}_1F_1\left(-\frac{m^2}{4}+\frac{1}{4},\frac{1}{2},m^2x^2\right)$ and through orthoganality (Stourm-Liouiville theorem) obtain coefficients:

$$C_m = -C^*\frac{\int_{x=0}^{1}(1-x^2)e^{-m^2x^2/2}{}_1F_1\left(-\frac{m^2}{4}+\frac{1}{4},\frac{1}{2},m^2x^2\right)\mathrm{d}x}{\int_{x=0}^{1}(1-x^2)e^{-m^2x^2/2}{}_1F_1\left(-\frac{m^2}{4}+\frac{1}{4},\frac{1}{2},m^2x^2\right)^2\mathrm{d}x} \tag{62}$$

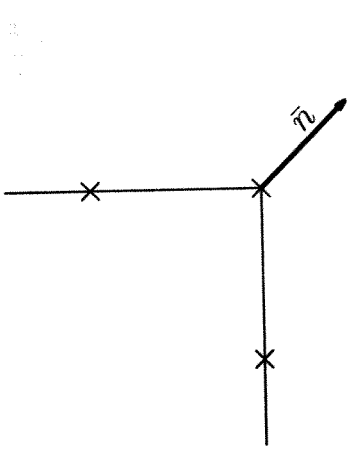

Figure 19: Free-surface boundary condition represented in the lattice Boltzmann. By crosses we outline boundary nodes, by circle the fluid node is outlined. Populations at the corner boundary nodes are essentially the population of the fluid node, but in the certain order.

Therefore a whole solution can be written as:

$$C = C^* - C^* \sum_{m=0} C_m e^{-m^4 \frac{x}{\delta} \frac{1}{Pe}} e^{-m^2 y^2/(2\delta^2)} {}_1F_1\Big(-\frac{m^2}{4} + \frac{1}{4}, \frac{1}{2}, m^2 \frac{y^2}{\delta^2}\Big), \quad (63)$$

where coefficients C_m are taken from Eq. 62. For the case C^*, first ten coefficients equal to 1.2008, −0.2991, 0.1608, −0.1074, 0.0796, −0.0627, 0.0515, −0.0435, 0.0375, −0.0329.

C Free surface boundary conditions

There are a few implementations of free boundary conditions [47, 48]. However, we developed the easy solver to impose the free surface boundary conditions at the complicated surface of the bubble. The reason is to impose the symmetric boundary conditions. Because the boundary is the staircase approximation, one can find the normal to the boundary which is always located by the angle of multiple of 45 degrees, see Fig. 19. This can be done automatically by the' simple coding. Imposing the symmetric boundary conditions requires $U_{n,F}$=$U_{n,B}$ and $U_{\tau,F} = U_{\tau,B}$. We can copy populations in the certain order to do it, for example $f_{B,i} = f_{F,\bar{i}}$, where c_i and $c_{\bar{i}}$ are complementary directions, where $c_{i,n} = -c_{\bar{i},n}$ and $c_{i,\tau} = c_{\bar{i},\tau}$, where $c_{i,n} = (\boldsymbol{c_i} \cdot \boldsymbol{n})\boldsymbol{n}$ and $c_{i,\tau} = \boldsymbol{c_i} - (\boldsymbol{c_i} \cdot \boldsymbol{n})\boldsymbol{n}$.

References

[1] M.D. Giavedoni and F.A. Saita. The axisymmetric and plane cases of a gas phase steadily displacing a Newtonian liquid - A simultaneous solution of the governing equations. *Phys. Fluids*, 9(8):2420–2428, 1997.

[2] J.J. Derksen. Simulations of lateral mixing in cross-channel flow. *Comput. Fluids*, 39:1058–1069, 2010.

[3] J.M. van Baten and R. Krishna. CFD simulations of mass transfer from Taylor bubbles rising in circular capillaries. *Chem. Eng. Sc.*, 59:2535–2545, 2004.

[4] M.T. Kreutzer, F. Kapteijn, J.A. Moulijn, and J.J. Heiszwolf. Multiphase monolith reactors: Chemical reaction engineering of segmented flow in microchannels. *Chem. Eng. Sci.*, 60:5895–5916, 2005.

[5] G. Bercic and A. Pintar. The role of gas bubbles and liquid slug lengths on mass transport in the Taylor flow through capillaries. *Chem. Eng. Sci.*, 52(21-22):3709–3719, 1997.

[6] F.P. Bretherton. The motion of long bubbles in tubes. *J Fluid Mech.*, 10 (2):166–188, 1960.

[7] G.I. Taylor. Deposition of a viscous fluid on the wall of a tube. *J. Fluid Mech.*, 10:161–165, 1961.

[8] J. Yue, L. Luo, Y. Gonthier, G. Chen, and Q. Yuan. An experimental study of air-water Taylor flow and mass transfer inside square microchannels. *Chem. Eng. Sci.*, 64:3697–3708, 2009.

[9] R. Gupta, D.F. Fletcher, and B.S. Haynes. Taylor Flow in Microchannels: A Review of Experimental and Computational Work. *J. Comput. Multiphase Flows*, 2:1–32, 2010.

[10] M.T. Kreutzer, M.G. van der Eijnded, F. Kapteijn, J.A. Moulijn, and J.J. Heiszwolf. The pressure drop experiment to determine slug lengths in mulitphase monoliths. *Catalysis Today*, 105:667–672, 2005.

[11] W.B. Kolb and R.L. Cerro. Film Flow in the Space between a Circular Bubble and a Square tube. *J. Coll. Int. Sci.*, 159:302–311, 1993.

[12] T.C. Thulasidas, M.A. Abraham, and R.L. Cerro. Bubble-train flow in capillaries of circular and square cross section. *Chem. Eng. Sci.*, 50(2): 183–199, 1995.

[13] D. Liu and S. Wang. Hydrodynamics of Taylor flow in noncircular capillaries. *Chem. Eng. and Processing*, 47:2098–2106, 2008.

[14] A. Kuzmin, M. Januszewski, D. Eskin, F. Mostowfi, and J. Derksen. Three-dimensional binary-liquid lattice boltzmann simulation of microchannels with rectangular cross sections. *Chem. Eng. J.*, 178:306–316, 2011.

[15] A.L. Hazel and M. Heil. The steady propagation of a semi-infinite bubble into a tube of elliptical or rectangular cross-section. *J. Fluid Mech.*, 470: 91–114, 2002.

[16] S. Irandoust and B. Ertle, S. adn Andersson. Gas-Liquid Mass Transfer in Taylor Flow Through a Capillary. *Canadian J. Chem. Eng.*, 70:115–119, 1992.

[17] R. Higbie. The rate of absorption of a pure gas into a still liquid during short periods of exposure. *Trans. Amer. Inst. Chem. Eng.*, 31:365–389, 1935.

[18] A. Kuzmin, M. Januszewski, D. Eskin, F. Mostowfi, and J. Derksen. Simulations of gravity-driven flow of binary liquids in microchannels. *Chem. Eng. J.*, 171(2):646–654, 2011.

[19] U. Frisch, D. d'Humieres, B. Hasslacher, P. Lallemand, Y. Pomeau, and J.-P. Rivet. Lattice gas hydrodynamics in two and three dimensions. *Complex Systems*, 1:649–707, 1987.

[20] G.R. McNamara and G. Zanetti. Use of the Boltzmann Equation to Simulate Lattice-Gas Automata. *Phys. Rev. Lett.*, 61(20):2332–2335, 1988.

[21] F.J. Higuera and J. Jimenez. Boltzmann Approach to Lattice Gas Simulations. *Europhys. Lett.*, 9(7):663–668, 1989.

[22] F.J. Higuera, S. Succi, and R. Benzi. Lattice gas dynamics with enhanced collisions. *Europhys. Lett.*, 9(4):345–349, 1989.

[23] D. Yu, R. Mei, L.-S. Luo, and W. Shyy. Viscous flow computations with the method of lattice Boltzmann equation. *Progress in Aerospace Sciences*, 39:329–367, 2003.

[24] X. Shan and H. Chen. Simulation of nonideal gases and gas-liquid phase transitions by the lattice Boltzmann Equation. *Phys. Rev. E*, 49(4):2941–2948, 1994.

[25] M.R. Swift, W.R. Osborn, and J.M. Yeomans. Lattice Boltzmann Simulation of Nonideal Fluids. *Phys. Rev. Lett.*, 75(5):831–834, 1995.

[26] A.K. Gunstensen, D.H. Rothman, S. Zaleski, and G. Zanetti. Lattice Boltzmann model of immiscible fluids. *Phys. Rev. A*, 43(8):4320–4327, 1991.

[27] P. Yuan and L. Schaefer. A Thermal Lattice Boltzmann Two-Phase Flow Model and Its Application to Heat Transfer Problems -Part 2. Integration and Validation. *J. Fluids Eng.*, 128:151–156, 2006.

[28] R. Zhang and H. Chen. Lattice Boltzmann method for simulations of liquid-vapor thermal flows. *Phys. Rev. E*, 67(066711):1–6, 2003.

[29] P.J. Dellar. Lattice Kinetic Formulation for Ferrofluids. *J. Stat. Phys.*, 121:105–118, 2005.

[30] G. Falcucci, G. Chiatti, S. Succi, A.A. Mohamad, and A. Kuzmin. Rupture of a ferrofluid droplet in external magnetic fields using a single-component lattice Boltzmann model for nonideal fluids. *Phys. Rev. E*, 79(056706):1–5, 2009.

[31] I. Ginzburg. Equilibrium-type and link-type lattice Boltzmann models for generic advection and anisotropic-dispersion equation. *Adv. Wat. Res.*, 28: 1171–1195, 2005.

[32] I. Ginzburg. Generic boundary conditions for lattice Boltzmann models and their application to advection and anisotropic dispersion equations. *Adv. Wat. Res.*, 28:1196–1216, 2005.

[33] I. Ginzburg. Variably saturated flow described with the anisotropic Lattice Boltzmann methods. *Comput. Fluids*, 35:831–848, 2006.

[34] M. Yoshino and T. Inamuro. Lattice Boltzmann simulations for flow and heat/mass transfer problems in a three-dimensional porous structure. *Int. J. Num. Meth. Fluids*, 43:183–198, 2003.

[35] P. L. Bhatnagar, E. P. Gross, and M. Krook. A Model for Collision Processes in Gases. I.Small Amplitude Processes in Charged and Neutral One-Component Systems. *Phys. Rev.*, 94(3):511–525, 1954.

[36] I. Ginzburg, F. Verhaeghe, and D. d'Humières. Two-relaxation-time Lattice Boltzmann scheme: about parametrization, velocity, pressure and mixed boundary conditions. *Commun. Comput. Phys.*, 3(2):427–478, 2008.

[37] I. Ginzburg and D. d'Humières. Multireflection boundary conditions for lattice Boltzmann models. *Phys. Rev. E*, 68(066614):1–30, 2003.

[38] I. Ginzburg. Lattice Boltzmann modeling with discontinious collision components: Hydrodynamic and Advection-Diffusion Equations. *J. Stat. Phys.*, 126(1):157–206, 2007.

[39] D. d'Humieres and I. Ginzburg. Viscosity independent numerical errors for Lattice Botlzmann models: From recurrence equations to "magic" collision numbers. *Comp. Math. Appl.*, 58(5):823–840, 2009.

[40] B. Servan-Camas and F. T.-C. Tsai. Lattice Boltzmann method with two relaxation times for advection-diffusion equation: Third order analysis and stability analysis. *Adv. Wat. Res.*, 31:1113–1126, 2008.

[41] I. Ginzburg. Consistent Lattice Boltzmann schemes for the Brinkman model of porous flow and infinite Chapman-Enskog expansion. *Phys. Rev. E*, 77(066704):1–12, 2008.

[42] I. Ginzburg, D. D'Humieres, and A. Kuzmin. Optimal Stability of Advection-Diffusion Lattice Boltzmann Models with Two Relaxation Times for Positive/Negative Equilibrium. *J. Stat. Phys.*, 139(6):1090–1143, 2009.

[43] A. Kuzmin, I. Ginzburg, and A.A. Mohamad. The role of the kinetic parameter in the stability of two-relaxation-time advection-diffusion lattice Boltzmann schemes. *Comp. Math. Appl.*, 61:3417–3442, 2011.

[44] S. Chapman and T.G. Cowling. *The mathematical theory of non-uniform gases.* Cambridge University Press, Cambridge, third edition, 1995.

[45] A.D. Polyanin, A.M. Kutepov, A.V. Vyazmin, and D.A. Kazenin. *Hydrodynamics, Mass and Heat Transfer in Chemical Engineering.* Taylor and Francis, 2002.

[46] M. Abramowitz and I. Stegun, editors. *Handbook of mathematical functions with formulas, graphs and mathematical tables.* National Bureau of Standards, 1964.

[47] I. Ginzburg and K. Steiner. A free-surface lattice Boltzmann method for modelling the filling of expanding cavities by Bingham fluids. *Phil. Trans. R. Soc. Lond. A*, 360:453–466, 2002.

[48] X. Yin, D.L. Koch, and R. Verberg. Lattice-Boltzmann method for simulating spherical bubbles with no tangential stress boundary conditions. *Phys. Rev. E*, 73:1–13, 2006.